Spring 5-25-2014

Low Noise, High Detectivity Photodetectors based on Organic Materials

Fawen Guo
University of Nebraska-Lincoln, fawen.guo@yahoo.com

Low Noise, High Detectivity Photodetectors based on Organic Materials

by

Fawen Guo

A DISSERTATION

Presented to the Faculty of

The Graduate College at the University of Nebraska

In Partial Fulfillment of Requirements

For the Degree of Doctor of Philosophy

Major: Engineering

Under the Supervision of Professor Jinsong Huang

Lincoln, Nebraska

May, 2014

Low Noise, High Detectivity Photodetectors based on Organic Materials

Fawen Guo, Ph.D.

University of Nebraska, 2014

Advisor: Jinsong Huang

Organic photodetectors (OPDs) are potentially useful in many applications because of their light weight, flexibility and good form factors. Despite the high detectivities that have been frequently reported for OPDs recently, the application of these OPDs for weak light detection has been rarely demonstrated.

In this thesis, low noise, high gain photodetectors based on organic and ZnO nanoparticles were proposed and demonstrated for highly sensitive UV light detection. The nanocomposite photodetector works in a hybrid mode of photodiode and photoconductor with the transition controlled by the UV light illumination. The nanocomposite detector shows two orders of magnitude higher sensitivity than silicon detectors in the UV range, which is the first time an organic, solution-processed detector has been shown to significantly outperform the inorganic photonic devices.

In the fullerene-based photodetector, the dark-current has been successfully reduced by a cross-linked TPD (C-TPD) buffer layer. The high detectivity of 3.6×10^{11} cm $\mathrm{Hz}^{\frac{1}{2}}\,\mathrm{W}^{-1}$ (Jones) at 370 nm and the wide Linear dynamic range (LDR) of 90 dB, along with a response speed faster than 20 kHz, suggests that the fullerene-based organic photodetectors proposed here can open the way for many potential applications.

The ZnO nanoparticles have been introduced into the C-TPD buffer layer of the fullerene-based photodetector to increase the photoconductive gain and reduce the noise current. The peak external quantum efficiency (EQE) value of approximately 400% and the peak specific detectivity of 6.5×10^{12} Jones at the wavelength of 390 nm, along with the record high LDR of 120 dB, enable the photodetector to be used in wide range of applications such as imaging, communication, and defense. The extremely high sensitivity of the photodetector also makes it particularly attractive for very weak light detection.

Acknowledgement

The research in this dissertation was carried out during my graduate study in the Department of Materials Engineering at the University of Nebraska - Lincoln. Many people helped me to complete this work.

First of all, I am very grateful to my advisor, Professor Jinsong Huang, who has a very solid background in materials engineering and wide research experience; most importantly, he always has good ideas in research. I thank him for giving me a chance to work with him and for his continued extraordinary support, valuable advice and encouragement. It is a great pleasure to be a member in this word-leading research group. It is my advisor's intelligent and very hard work that makes this group efficient and productive.

Secondly, I want to thank my committee members, Professor Jeffrey Shield, Professor Stephen Ducharme and Professor Yongfeng Lu for their time, interest and detailed critique on my comprehensive exam and this dissertation.

I would like to take this opportunity to thank my colleagues in this group for being supportive all the time, Dr. Yongbo Yuan, Yu Bi, Dr. Bin Yang, Dr. Rui Dong, Dr. Baodong Mao, Zhengguo Xiao, Shumin Li. Cheng Bi, Yuchuan Shao, Dr. Yanjun Fang, and Mrs. Jing Yu. Their professional expertise and collaboration are very crucial to all of my achievements.

I would like to thank our department staffs, Will McClure, Kathie Hiatt, Alicia Harvey, and Cheryl Wemhoff from Department of Electrical Engineering.

Last, but not the least, I gratefully thank my parents and parents in-law for their love, support and patience that enabled me to achieve my goals. Finally, I want to thank my beloved wife, Lijing Liu for her help, support, understanding and love.

This dissertation is also for my lovely son Owen and daughter Sophia: you two make my life beautiful and worthwhile.

This dissertation was supported by the Office of Naval Research (ONR, grant no. N000141210556), a Defense Threat Reduction Agency (DTRA) Young Investigator Award (HDTRA1-10-1-0098), and the University of Nebraska – Lincoln.

Table of Contents

LIST OF FIGURES

CHAPTER 1 INTRODUCTION

1.1 Background and Motivation

Ultraviolet (UV) detection is critical for a wide range of applications both in civilian and military areas, including medical instruments, missile flame detection, environmental and biological research, astronomical studies, optical communication, radiation detection and so on [1-6].

"UV-enhanced" silicon and GaN photodiodes are the most common devices for UV photodetection [7,8]. GaN detectors have superior performance with "visible-blindness" capability. They are sensitive to UV radiation but not to visible radiation. These single-crystalline detectors exhibit some inherent limitations. They are expensive and have low quantum efficiency (<40%, responsivity of <0.2 A/W). In addition, for very weak light sensing, silicon photodiodes need to be cooled to reduce the dark-current [9].

For ultra-weak light detection, preamplifiers are always needed to read the weak current signal [10], however, the amplifiers can bring new source of noise and also make the system more expensive. For these reasons, the photodetctors without an internal gain are not suitable for the detection of very low level light down to single photon level. Photodetectors with high internal gain, such as photomultiplier tubes (PMTs) [11] and avalanche photodiode (APDs) [12], are widely used for weak signal detection. More than one electron can be extracted out of these photodetectors for

each incident photon which contributes to the gain. However, these high gain photodetectors, such as APDs, generally need very high driving voltage of hundreds volts [13], which limits their applications greatly. It would be advantageous to have a low-cost UV photodetector with high quantum efficiency, high sensitivity, and quick response and does not require cooling to obtain high detectivity.

A critical method to make the low-cost photodetector has been made using colloidal inorganic semiconductor. PbS quantum dots were used by solution process to fabricate photodetectors onto gold interdigitated electrodes [14]. These photodetectors showed photoconductive gain with high responsivity greater than 1,000 A/W in the infrared range, yielding detectivity surpassing inorganic detectors due to the large gain and the reduced noise. However, in such kind of colloidal photodetectors, both the electrodes and the quantum dot semiconductor of the photoconductive detectors are all in one plane, with electrode spacing > 5 mm to reduce dark-current. As a result, in order to maintain the high gain, the detectors need a very high driving voltage of 100 V which cannot be provided by any commercially available thin film transistors [15].

The detection of weak light by organic semiconductor devices has recently attracted great attention due to their advantages of low cost, physical flexibility, large area coverage and easy integration with silicon readout circuit [16-18]. The wide range of bandgap tunability of organic semiconductor materials, synthesized by chemical process, provide tremendous flexibility in the choice of materials for various detection applications with different responding spectra [19,20]. However, the

performances of these organic materials based UV photodetectors are still not comparable to the inorganic photodetectors.

In summary, it is still a big challenge to detect ultra-weak UV light with organic photdetectors. A new type of photodetector is in urgent need to obtain high sensitivity organic UV photodetectors.

In this thesis, a novel ZnO/polymer nanocomposite UV detector based on interfacial trap-controlled charge injection [21], and fullerene UV detectors with wide dynamic range were proposed [22,23]. These detectors have high sensitivity and low noise current, which make them perfect candidates for the weak UV light detection.

1.2 Tasks of Current Research

The tasks in this thesis include:

1. Develop a hybrid UV photodetector by nanocoposite materials with ZnO nanoparticles and polymers, reduce the dark-current, increase the response speed and detectivity; combine the low dark-current of the photodiode and high gain of the photoconductor;
2. Study the fullerene UV photodetecors and increase the detectivity by reducing the dark-current with a crosslinkable buffer layer;
3. Using a ZnO nanocomposite buffer layer in the fullerene-based UV photodetctor to get both a high gain and low dark-current for the weak light detection.

1.3 Thesis Outline

In this thesis, highly sensitive, low noise UV photodetectors based on organic and ZnO nanoparticles were proposed and fabricated. Their performances were characterized and the working principles were also discussed.

This thesis is organized into 6 chapters.

Chapter 1: INTRODUCTION. This chapter covers the backgrounds and motivations of the photodetectors and an outline of this thesis.

Chapter 2: BACKGROUND AND REVIEWS. This chapter describes backgrounds reviews of current research progress.

Chapter 3: ZnO/POLYMER NANOCOMPOSITE UV PHOTODETECTOER. This chapter presents highly sensitive nanocomposite UV photodetector based on interfacial trap-controlled charge injection.

Chapter 4: FULLEREN PHOTODETECTORS WITH WIDE LINEAR DYNAMIC RANGE. This chapter reports a fullerene photodetector with wide linear dynamic range enabled by C-TPD buffer layer.

Chapter 5: LARGE GAIN, LOW NOISE NANOCOMPOSITE ULTRAVIOLET PHOTODETECTORS**.** This chapter reports a photodetector made with nanocmposite/fullerene with large gain and low noise.

Chapter 6: SUMMARY AND FUTURE WORK. This chapter summarizes this thesis and also provides some suggestions for future works.

1.4 References

[1] Monroy, E., Calle, F., Pau, J., Munoz, E., Omnes, F., Beaumont, B. & Gibart, P. AlGaN-based UV photodetectors. *Journal of crystal growth* **230**, 537-543 (2001).

[2] Li, J., Fan, Z., Dahal, R., Nakarmi, M., Lin, J. & Jiang, H. 200 nm deep ultraviolet photodetectors based on AlN. *Applied Physics Letters* **89**, 213510 (2006).

[3] Sharma, P. & Sreenivas, K. Highly sensitive ultraviolet detector based on ZnO/LiNbO 3 hybrid surface acoustic wave filter. *Applied Physics Letters* **83**, 3617-3619 (2003).

[4] Hoshino, T., Senda, M., Hondo, T., Saito, M. & Tohei, S. Application of photodiode array ultraviolet detector to unresolved peak analysis. *Journal of Chromatography A* **316**, 473-486 (1984).

[5] Morton, D. C. & Purcell, J. D. Observations of the extreme ultraviolet radiation in the night sky using an atomic hydrogen filter. *Planetary and Space Science* **9**, 455-458 (1962).

[6] Gottwald, A., Kroth, U., Richter, M., Schöppe, H. & Ulm, G. Ultraviolet and vacuum-ultraviolet detector-based radiometry at the Metrology Light Source. *Measurement Science and Technology* **21**, 125101 (2010).

[7] Streltsov, A. M., Moll, K., Gaeta, A. L., Kung, P., Walker, D. & Razeghi, M. Pulse autocorrelation measurements based on two-and three-photon

conductivity in a GaN photodiode. *Applied Physics Letters* **75**, 3778-3780 (1999).

[8] Van Hove, J., Hickman, R., Klaassen, J., Chow, P. & Ruden, P. Ultraviolet-sensitive, visible-blind GaN photodiodes fabricated by molecular beam epitaxy. *Applied Physics Letters* **70**, 2282-2284 (1997).

[9] Gruber, G., Moses, W., Derenzo, S., Wang, N., Beuville, E. & Ho, H. A discrete scintillation camera module using silicon photodiode readout of CsI (TI) crystals for breast cancer imaging. *Nuclear Science, IEEE Transactions on* **45**, 1063-1068 (1998).

[10] Park, H., Kuo, Y.-h., Fang, A. W., Jones, R., Cohen, O., Paniccia, M. J. & Bowers, J. E. A hybrid AlGaInAs-silicon evanescent preamplifier and photodetector. *Optics express* **15**, 13539-13546 (2007).

[11] Dolgoshein, B., Balagura, V., Buzhan, P., Danilov, M., Filatov, L. *et al.* Status report on silicon photomultiplier development and its applications. *Nuclear Instruments and Methods in Physics Research Section A: Accelerators, Spectrometers, Detectors and Associated Equipment* **563**, 368-376 (2006).

[12] Emmons, R. Avalanche‐Photodiode Frequency Response. *Journal of applied physics* **38**, 3705-3714 (2004).

[13] Liu, J.-M. *Photonic Devices*. 966-986 (Cambridge University Press, 2005).

[14] McDonald, S. A., Konstantatos, G., Zhang, S., Cyr, P. W., Klem, E. J., Levina, L. & Sargent, E. H. Solution-processed PbS quantum dot infrared photodetectors and photovoltaics. *Nature Materials* **4**, 138-142 (2005).

[15] Konstantatos, G., Howard, I., Fischer, A., Hoogland, S., Clifford, J., Klem, E., Levina, L. & Sargent, E. H. Ultrasensitive solution-cast quantum dot photodetectors. *Nature* **442**, 180-183 (2006).

[16] Lin, H. W., Ku, S. Y., Su, H. C., Huang, C. W., Lin, Y. T., Wong, K. T. & Wu, C. C. Highly Efficient Visible‐Blind Organic Ultraviolet Photodetectors. *Advanced Materials* **17**, 2489-2493 (2005).

[17] Ray, D. & Narasimhan, K. High response organic visible-blind ultraviolet detector. *Applied Physics Letters* **91**, 093516 (2007).

[18] Peumans, P., Yakimov, A. & Forrest, S. R. Small molecular weight organic thin-film photodetectors and solar cells. *Journal of applied physics* **93**, 3693-3723 (2003).

[19] Katz, H., Lovinger, A., Johnson, J., Kloc, C., Siegrist, T., Li, W., Lin, Y.-Y. & Dodabalapur, A. A soluble and air-stable organic semiconductor with high electron mobility. *Nature* **404**, 478-481 (2000).

[20] Hill, I., Rajagopal, A., Kahn, A. & Hu, Y. Molecular level alignment at organic semiconductor-metal interfaces. *Applied Physics Letters* **73**, 662-664 (1998).

[21] Guo, F., Yang, B., Yuan, Y., Xiao, Z., Dong, Q., Bi, Y. & Huang, J. A nanocomposite ultraviolet photodetector based on interfacial trap-controlled charge injection. *Nature Nanotechnology* **7**, 798-802 (2012).

[22] Guo, F., Xiao, Z. & Huang, J. Fullerene Photodetectors with a Linear Dynamic Range of 90 dB Enabled by a Cross‐Linkable Buffer Layer. *Advanced Optical Materials* **1**, 289-294 (2013).

[23] Fang, Y., Guo, F., Xiao, Z. & Huang, J. Large Gain, Low Noise Nanocomposite Ultraviolet Photodetectors with a Linear Dynamic Range of 120 dB. *Advanced Optical Materials* (2014).

CHAPTER 2 BACKGROUND AND REVIEWS

In this chapter, the backgrounds of photodetectors are described. The UV photodetectors based on ZnO nanostructures and organic materials are briefly reviewed. Current challenges are also discussed in the end.

2.1 Introduction of Photodetector

A photodetector is a device that converts an optical signal into another kind of signal, such as electrical signal in the form of current or voltage [1]. In this thesis, we are only focused on the semiconductor photodetetors. The working mechanism of them is based on the photoelectric effect, i.e. they absorb the photon energy and then generate electron-hole pairs.

According to their different working mechanisms or device structures, Photodetectors can be divided into several groups, such as photoconductors, junction photodiodes, phototransistors, and charge-coupled devices (CCDs), etc.

The typical photodetector performance parameters were summarized as below; more details were discussed in the following chapters of 3, 4 and 5.

Spectral Response: For any given photodetectrors, they can only respond to a specific wavelength range. When designing a photodetetor, the first consideration is choosing the proper material that can respond to the photo signal. In this thesis, we only focused on ultraviolet photodetectors.

External Quantum Efficiency（EQE）: EQE can be defined as the ratio of the number of photogenerated charge carriers, in the form of either photoelectrons or electron–hole pairs, to the number of incident photons. EQE has the same numerical value as gain. For example, we can say the gain is 10 when EQE is 1000%. However, the term of gain is generally used when EQE is larger than 100%; If EQE < 100%, we say there is no gain.

Responsivity(R): Responsivity is defined as the ratio of the output current or voltage signal to the power of the input optical signal. It is an important parameter and can tell us the available output signal of a detector for a given input signal.

Noise Equivalent Power (NEP): The noise equivalent power is defined as the input power required of the input signal for the signal-to-noise ratio (SNR) to be unity at the detector output. It is the minimum power needed to distinguish a signal from the noise. A photodetector with smaller NEP can detect weaker light than the photodetector with larger NEP.

Detectivity: The detectivity characterizes the ability of a photodetector to detect a small photo signal. It equals to the inverse of the NEP of the detector.

Linearity and Dynamic Range (LDR): Linearity of a photodetector means that its output signal is linearly proportional to its input optical signal. We need a large LDR to detect both the weak and strong light.

Response Speed: A photodetector should be fast enough to follow the input optical signal. The response speed is characterized by the rise time and the fall time of its response to an impulse signal or to a square-pulse signal, as shown in Fig.2.1 [1].

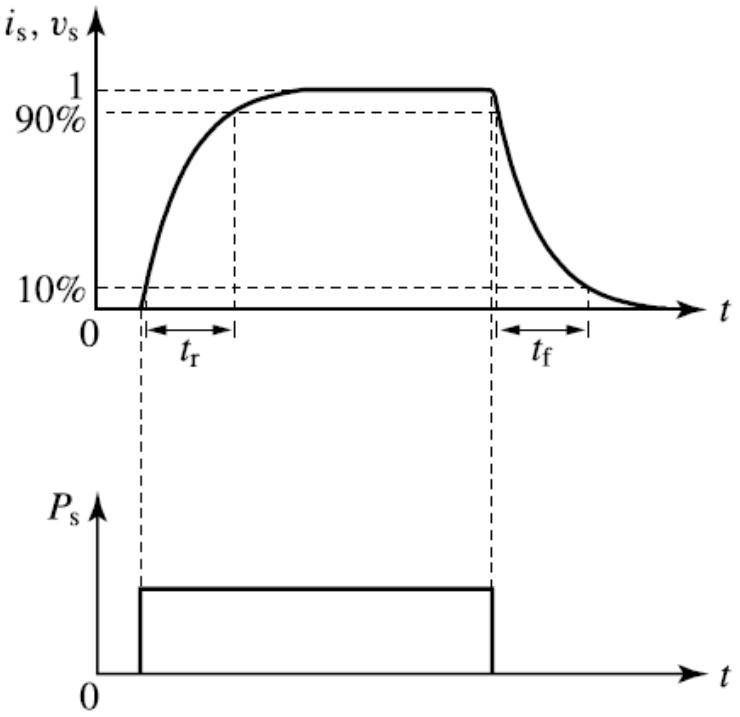

Figure 2. 1 Rise time (t_r) and fall time (t_f) of a photodetector with a square-pulse signal.

For the ultraviolet photodetection, numerous kinds of materials and device structures were utilized in the past decades. Here, we summarized some recent progress on the ultraviolet detection based on ZnO nanostructure materials and organic materials.

2.2 ZnO-Nanostructure-Based Ultraviolent Photodetectors

2.2.1 Photoconductors

Photoconductor, also called photoresistor or light-dependent resistor, is based on the phenomenon of photoconductivity. It becomes more conductive due to the absorption of electromagnetic radiation, such as ultraviolet light and visible light. They have large resistance in the dark and high conductance under suitable

illumination with photon energy higher than the bandgap of the semiconductors. The typical photoconductor usually has a semiconductor layer sandwiched by two ohmic contacts. This kind of photodetectors can have high photoconductive gain and high responsivity, so they don't need any external amplifying equipment, such as the photomultiplier tube. However, they have relatively large dark-current, small linear dynamic range, and slow response speed. Many efforts have been taken to solve these issues, such as using nanoparticles [2,3] or, surface treatment [4,5].

One dimensional ZnO Nanowires (NW) or nanobelts have attracted more attention due to the large surface-to-volume ratio [6]. The photocarrier lifetime and charge trap density can be enlarged significantly by this large surface to volume ratio. This kind of photodetector usually has high quantum efficiency and high sensitivity. Fig.2.2 shows a high gain ZnO nanorod UV photodetector reported by Soci. C *et al.* [7]. Upon illumination with photon energy above the bandgap, electron hole pairs are generated and holes are trapped at the surface. The electrons are collected at the anode under an applied electric field. The high photoconductive gain of 10^8 is attributed to the presence of oxygen-related hole-trap states at the NW surface, which prevents charge-carrier recombination and prolongs the photocarrier lifetime.

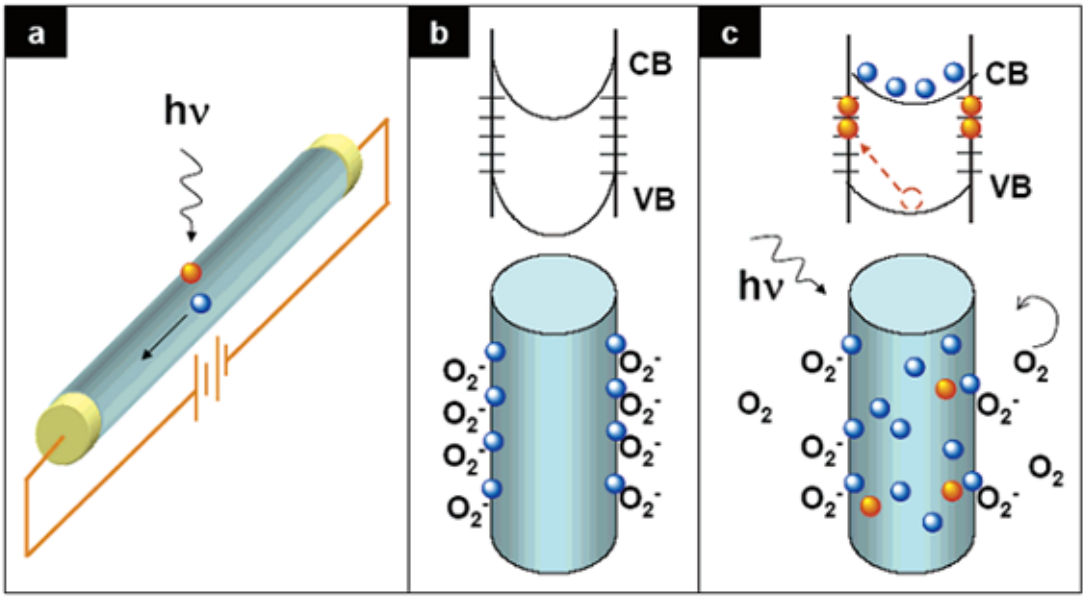

Figure 2. 2 Photoconduction in NW photodetectors. (a) Schematic of a NW photoconductor； the top drawing in (b) shows the schematic of the energy band diagrams of a NW in the dark, The bottom drawing shows oxygen molecules adsorbed at the NW surface that capture the free electron present in the n-type semiconductor forming a low-conductivity depletion layer near the surface. (c) Under UV illumination, photogenerated holes migrate to the surface and are trapped, leaving behind unpaired electrons in the NW that contribute to the photocurrent [7].

However, photodetectors based on ZnO NWs mostly show a slow response speed because of the inherent defects, such as oxygen vaccines. Hu, L.F. *et al*. reported a biaxial nanobelts composed of ZnO and ZnS recently [8]. The detector was constructed by standard lithography procedures, the diameters of the ZnO/ZnS nanobelts varying from several tens of nm to 100 nm and up to tens of micrometers in length; a pair of 10 nm/100 nm Cr/Au electrodes with 3 μm apart is deposited on the ZnS/ZnO nanobelt dispersed at a SiO_2 /Si substrate (Fig.2.3). Ohmic contact was formed at the interface between ZnO/ZnS nanobelts and Cr/Au electrodes. This biaxial nanobelts photodetector has a high responsivity of 5.0×10^5 A/W and high EQE of 2.0×10^8 % irradiated by 320 nm light with a bias of 5.0 V. These high

performances are attributed to the formation of a type-II heterostructure with a staggered alignment at the heterojunction. There is a spatial separation of the photogenerated carriers due to the internal field at the ZnS/ZnO interface. This spatial separation can decrease the hole-electron pairs recombination, thus the photocurrent and EQE can be improved significantly. However, the detectivity and linearity are not mentioned in this report.

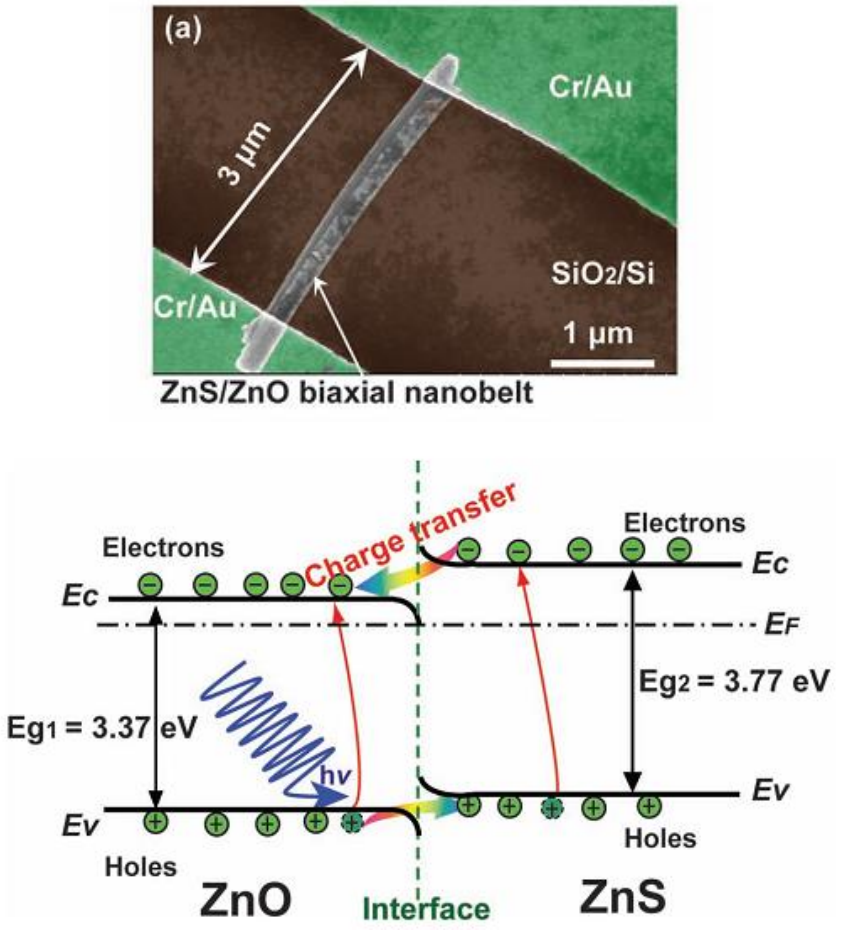

Figure 2. 3 SEM image and energy band diagram of the ZnS/ZnO nanobelt Photodetector.

Surface plasmons effect in nanostructured metals have also been found useful for improving the performance of photodetectors [9]. For example, by coating ZnO nanowire with Au nanoparticles (Fig.2.4), the dark-current decreased by 2 orders due

to the Au nanoparticles which can further deplete the carriers near the surface of ZnO nanowires and increase the width of depletion layer. Au nanoparticle-induced light scattering can increase the light absorption efficiency, so the ratio of photo current to dark-current increased from 10^3 to 5×10^6. Furthermore, the fall-time of the detector has been reduced from 300 s to 10 s by Au nanoparticles [3].

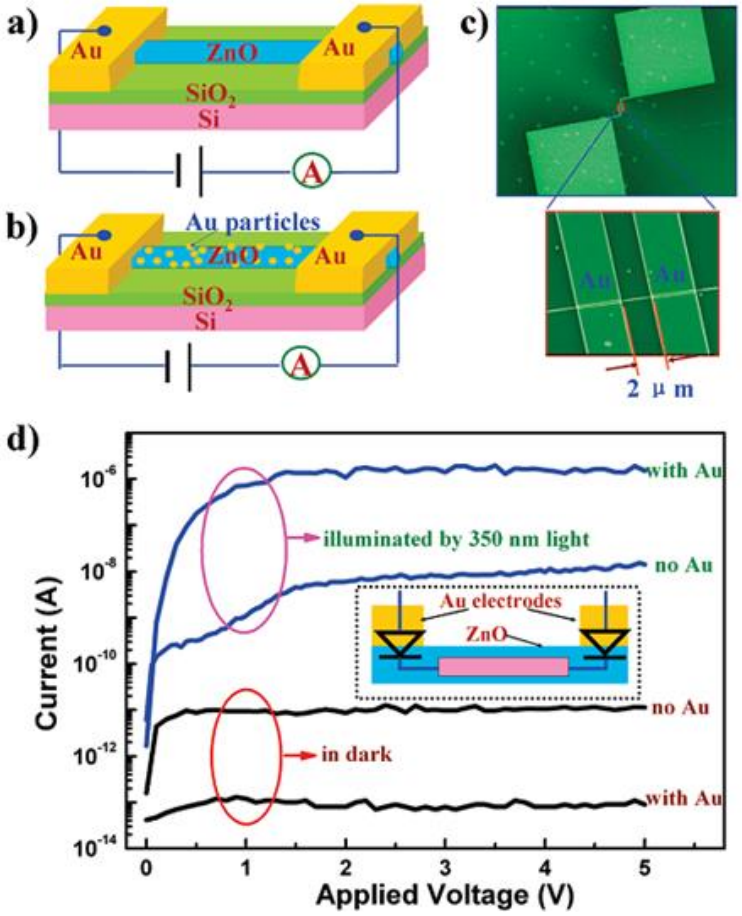

Figure 2. 4 Schematic of ZnO nanowire photodetectors without (a) and with (b) Au nanoparticles. (c) SEM image of the device. (d) I-V characteristics of ZnO nanowire photodetectors both in dark and under 350 nm UV light illumination. The inset of (d) is the equivalent circuit for the devices.

As discussed above, for the fabrication of one dimensional ZnO photodetectors sophisticated techniques such as photolithography, electron beam lithography, focused

ion beam or bridging nanostructures by lateral growth from one electrode to the other are needed [10]. These processes are complicated and uneconomic.

More recently, Hao,Y.H. *et al*. developed a new and cost-effective method to make UV photodetectors based on spatial network of tetrapod ZnO nanostructures [11]. The tetrapod ZnO nanostructures were first synthesized by thermal evaporation method. Au film was deposited on glass plate assisted by a metal mask, and a gap was scratched out with a width of 20 μm on the Au film to form a pair of electrodes by a special probe. The ZnO nanostructures were dispersed into the ethanol solution, and the solution was transferred to the area between the electrodes and allowed to dry in air. At last, spatial network of tetra-pod ZnO nanostructures was connected with two Au electrodes. Through this method, they got a sensitive detector with photocurrent to dark-current ratio of 4.5×10^5; the decay time is 0.3 s.

Li, Y.B. *et al*. reported another simple method that could fabricate electrodes and ZnO nanowires bridging the electrodes simultaneously in a single-step chemical vapor deposition (CVD) process. The device showed drastic changes ($10–10^5$ times) in current under a wide range of UV irradiances ($10^{-8}–10^{-2}$ Wcm^{-2}) [12].

2.2.2 Photodiodes

Photodiode photodetectors have at least one blocking contact, and are the most commonly used detectors in industry. They have many different types, such as Schottky photodiodes, p-n junction photodiodes, Metal-Semiconductor-Metal (MSM) photodiodes, etc. Compared with photoconductor; photodiode detectors have low

dark-current, fast response and wide linear dynamic range [5]. However, the gain usually cannot be higher than 1 because one photon can generate only one electron-hole pair and there is no charge injection under reverse bias.

2.2.2.1 Schottky photodiodes

Das. *et al*., compared single nanowire UV detectors with Schottky contact and Ohmic contact respectively [13]. For the device with Schottky contact, the photoexcited electron-hole pairs can greatly increase the concentration of majority carriers. It was concluded that the barrier height is strongly modulated by the UV exposure in the Schottky diode. The photocurrent to dark-current ratio is 75 for the Schottky diode, which is superior to a detector with ohmic contacts only.

In order to further improve sensitivity and response speed, the ZnO bascule nanobridges (NB) photodetectors with double Schottky contacts were reported [14]. The bascule NB structure consists of two cross-bridged ZnO NWs creating a junction; a double Schottky barrier is formed due to the surface depletion. The height of the double Schotty barrier can be modulated by UV illumination. It has a high barrier height in the dark and results in low dark-current. A photocurrent to dark-current ratio of 10^4 and a recovery time of 3 s was obtained by this structure.

Solution-processed optoelectronic devices have some advantages over conventional crystalline semiconductor devices due to ease of fabrication, large area, physical flexibility, and low cost [15,16]. Jin, Y.Z. *et al*. developed a

solution-processed UV photodetector based on colloidal ZnO nanoparticles [17]. Colloidal ZnO nanoparticles were first spin coated on glass substrates, followed by annealing in air and evaporation of Au contacts through a shadow mask (Fig.2.5). ZnO nanoparticles and Au forms a Schottky contact, which enabled a high resistance of 1 TΩ in the dark. The responsivity of the device has been determined to be approximately 61 A/W. The photocurrent is associated with a light-induced desorption of oxygen from the ZnO nanoparticle surfaces, thus removing electron traps and increasing the free carrier density which in turn reduces the Schottky barrier for electron injection. These solution-processed devices are promising for large-area UV photodetector applications; however, a high driving voltage of above 100 V is needed to get a high responsivity, which limits their applications significantly.

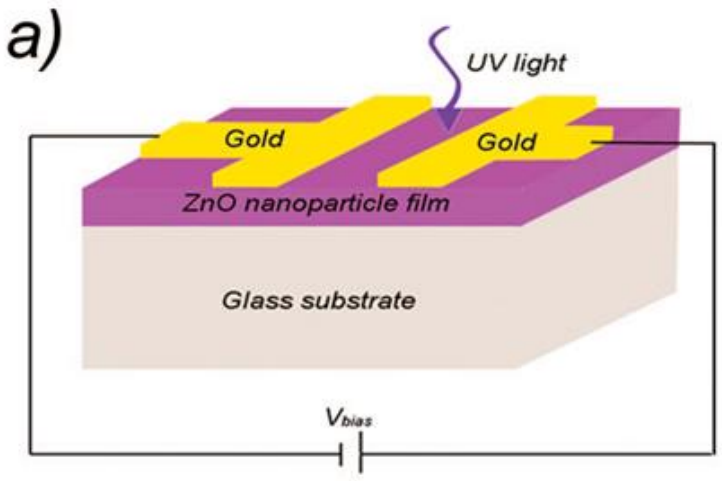

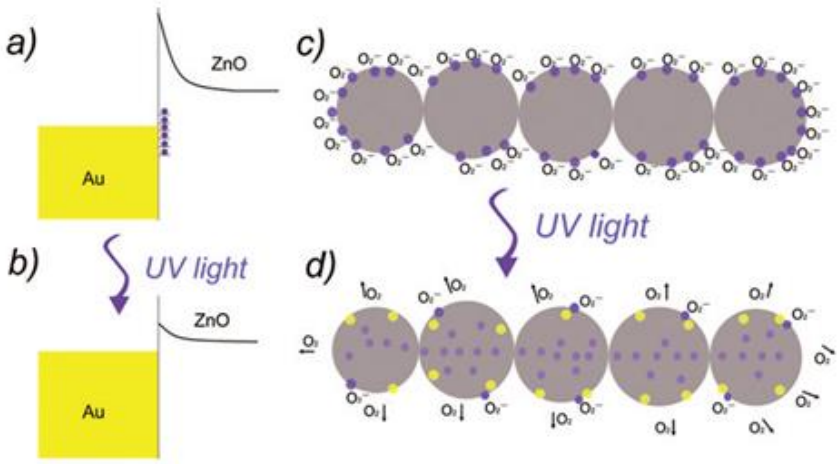

Figure 2. 5 Top (a) Schematic of a ZnO nanoparticle film device structure; Bottom (a,b) Schottky barriers formed at the gold/ZnO nanoparticle interfaces in the dark and under UV illumination, respectively. (c,d) Charge carrier trapping and transport in the ZnO nanoparticle films in the dark and under UV illumination, respectively.

2.2.2.2 p-n junction photodiodes

Chen, C.H. *et al.* reported a p–n heterojunction photodetector fabricated by ZnO NWs/p-GaN [18]. The synthesis of ZnO nanowires was initiated on p-GaN substrate by thermal chemical vapor deposition. The electron-hole pairs are generated in the array of ZnO nanowires when illuminated with UV light and are separated by the internal electric field. The device has a reverse leakage current of 3.7768×10^{-6} A in the dark. The photo current was almost 15 times higher than the dark-current.

Bie,Y.Q. *et al.* reported a self-powered UV detector based on ZnO/GaN Nanoscale p-n Junctions [19]. The heterojunction is based on a single n-type ZnO nanowire and a p-type GaN film. The detector was driven by the photovoltaic effect of the ZnO/GaN p-n junction. The ZnO/GaN junction showed significant rectification characteristics in the dark. The device could function as a self-powered UV detector

with an on-off ratio larger than 10^6 and it has a fast response speed with a decay time of 219 μ s.

In the last page of this chapter, some recent results based on ZnO nanostructures were summarized in table 2.1.

2.3 Organic Ultraviolet Photodetectors

Ultraviolet photodetectors are conventionally made with wide-bandgap inorganic semiconductors, such as III-nitrides and SiC [20-23]. However, their fabrication process is still complicated and expensive and therefore is not suitable for large-area applications. On the contrary, organic semiconductor devices, such as organic light emitting diodes [24], organic solar cells [25], organic transistors [26], and organic photodetectors [27], have developed rapidly in past years. Organic devices have the advantages of low fabrication cost, large-area scalability, and variety in substrates, making them attractive for large area or portable electronics. Although many organic materials have large band gaps and strong absorption in the UV range, and therefore have high potential for UV detection, organic ultraviolet photodetectors still have limited performances, compared to the inorganic ultraviolet photodetectors.

Debdutta, Ray. *et al*. reported a high efficiency visible-blind ultraviolet organic photodetector with a peak response of 30 mA/W [28]. The active layer is a blend of TPD and Alq_3 by coevaporating on prepatterned ITO glass substrates in vacuum. The authors show that the spontaneous and the electric field induced carrier generation efficiencies in the blend are enhanced over its constituents. The spontaneous carrier

generation efficiency is 30% in the blend. The photoluminescence of the blend shows an efficient energy transfer from the TPD to Alq_3. The responsivity of 30 mA/W compares favorably with the response of GaN (150 mA/W) and SiC(120 mA/W) based UV detector [29,30].

Zhanlin, Xu. *et al*. demonstrated a high response visible-blind organic ultraviolet photodetector using 4,4 ,4-tris[3-methyl-pheny(phenyl)amino]triphenylamine (m-MTDATA) and a Cu(I) complex, [Cu(1,2-bis(diphenylphosphino)benzene)(bathocuproine)]BF4 (CuBB) as the electron donor and acceptor, respectively(Fig.2.6). The photodetector shows a photocurrent up to 173A/cm^2 at −10 V, corresponding to a response of 251 mA/W under an illumination of 365 nm light. The high response is attributed to the high electron transport ability of CuBB, the suppression of radiative decay of m-MTDATA and efficient charge transfer from m-MTDATA to CuBB [31].

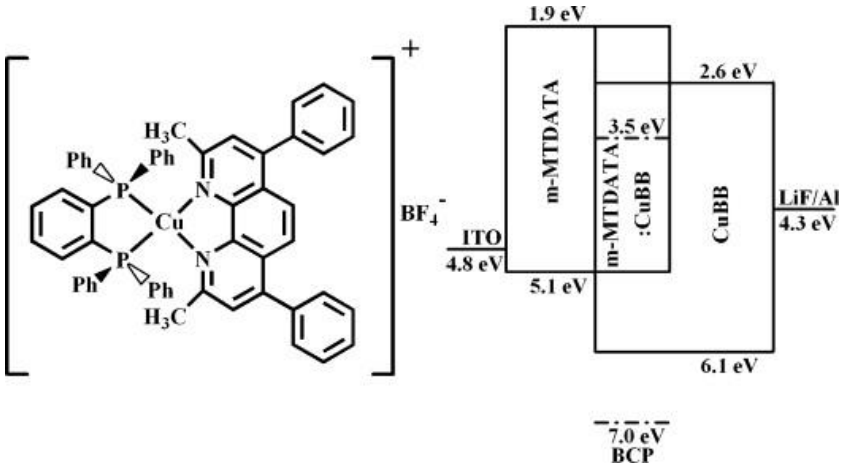

Figure 2. 6 Chemical structure of CuBB and schematic energy level diagram of UV-Photodetectors based on CuBB and BCP.

2.4 Challenges

As stated above, photodiode detectors can have a fast response speed and usually have a wide linear dynamic range and low noise, however, their gain cannot be higher than 1. Unlike photodiodes, photoconductors can have a high gain more than 1 and thus have higher detectivity than photodiodes. Many efforts have been put to improve the photoconductive gain, such as using solution-cast thin films of colloidal inorganic semiconductor nanoparticles or colloidal quantum dots as photoconductors. These kinds of photodetectors usally have lateral structures to increase shunt resistance and reduce dark-current, which lead to high driving voltage and low response speed. A combination of these two kinds of photodetectors is a promising direction for the further improvement of device performance. However, it is still a big challenge to make such a hybrid photodetector.

Table 2.1 ZnO nanostructure-based UV photodetectors

Type	**Voltage (V)**	**Wavelength (nm)**	**Gain**	**Responsivity (A/W)**	**Photo/dark current**	**Rise time**	**Decay time**	**Ref.**
Conductor	5	390	10^8	--	10^5	--	20 ns	[7]
Conductor	5	320	--	5×10^5	7	<0.3 s	1.7 s	[8]
Conductor	5	340	608	166	7×10^3	--	2.54 s	[10]
Conductor	1	365	--	--	4.5×10^5	0.4 s	0.3 s	[11]
Conductor	5	350	--	--	10^5	0.7 s	1.4 s	[12]
Diodes	< 5	352	--	--	75	<1 s	<1 s	[13]
Diodes	1	365	--	--	10^4	--	<0.12 s	[14]
Diodes	120	370	--	61	--	0.1 s	1.3 s	[17]
Diodes	5	365	--	--	15	--	--	[18]
Diodes	--	325	--	10^6	--	20 μs	219 μs	[19]
Conductor	5	365	--	--	2.5×10^5	< 1 s	< 1 s	[32]
Conductor	5	325	--	--	18	43.7 s	--	[33]
Conductor	5	365	--	6.2	90	5.9 s	638 s	[34]
Diodes	1	365	--	--	1500	0.6 s	6 s	[5]
Hybrids	9	360	3406	1001	10^7	< 25 μs	142 μs	[35]

2.5 References

[1] Liu, J.-M. *Photonic Devices, P 943*. (2005).

[2] Yuan, Y., Dong, Q., Yang, B., Guo, F., Zhang, Q., Han, M. & Huang, J. Solution-processed nanoparticle super-float-gated organic field-effect transistor as un-cooled ultraviolet and infrared photon counter. *Scientific reports* **3** (2013).

[3] Liu, K., Sakurai, M., Liao, M. & Aono, M. Giant improvement of the performance of ZnO nanowire photodetectors by Au nanoparticles. *The Journal of Physical Chemistry C* (2010).

[4] Lao, C. S., Park, M. C., Kuang, Q., Deng, Y., Sood, A. K., Polla, D. L. & Wang, Z. L. Giant enhancement in UV response of ZnO nanobelts by polymer surface-functionalization. *Journal of the American Chemical Society* **129**, 12096-12097 (2007).

[5] Zhou, J., Gu, Y., Hu, Y., Mai, W., Yeh, P. H., Bao, G., Sood, A. K., Polla, D. L. & Wang, Z. L. Gigantic enhancement in response and reset time of ZnO UV nanosensor by utilizing Schottky contact and surface functionalization. *Applied Physics Letters* **94**, 191103 (2009).

[6] Peng, L., Hu, L. & Fang, X. Low‐Dimensional Nanostructure Ultraviolet Photodetectors. *Advanced Materials* **25**, 5321-5328 (2013).

[7] Soci, C., Zhang, A., Xiang, B., Dayeh, S., Aplin, D., Park, J., Bao, X., Lo, Y. & Wang, D. ZnO nanowire UV photodetectors with high internal gain. *Nano letters* **7**, 1003-1009 (2007).

[8] Hu, L., Yan, J., Liao, M., Xiang, H., Gong, X., Zhang, L. & Fang, X. An Optimized Ultraviolet‐A Light Photodetector with Wide‐Range Photoresponse Based on ZnS/ZnO Biaxial Nanobelt. *Advanced Materials* **24**, 2305-2309 (2012).

[9] Atwater, H. A. & Polman, A. Plasmonics for improved photovoltaic devices. *Nature materials* **9**, 205-213 (2010).

[10] Peng, S. M., Su, Y. K., Ji, L. W., Wu, C. Z., Cheng, W. B. & Chao, W. C. ZnO Nanobridge Array UV Photodetectors. *The Journal of Physical Chemistry C* **114**, 3204-3208 (2010).

[11] Hao, Y., Zhao, J., Qin, L., Guo, Q., Feng, X. & Wang, P. Facile fabrication of UV photodetector based on spatial network of tetrapod ZnO nanostructures. (2012).

[12] Li, Y., Valle, F. D., Simonnet, M., Yamada, I. & Delaunay, J. J. High-performance UV detector made of ultra-long ZnO bridging nanowires. *Nanotechnology* **20**, 045501 (2009).

[13] Das, S. N., Moon, K. J., Kar, J. P., Choi, J. H., Xiong, J., Lee, T. I. & Myoung, J. M. ZnO single nanowire-based UV detectors. *Applied Physics Letters* **97**, 022103 (2010).

[14] Li, Y., Paulsen, A., Yamada, I., Koide, Y. & Delaunay, J. J. Bascule nanobridges self-assembled with ZnO nanowires as double Schottky barrier UV switches. *Nanotechnology* **21**, 295502 (2010).

[15] Huynh, W. U., Dittmer, J. J. & Alivisatos, A. P. Hybrid nanorod-polymer solar cells. *Science* **295**, 2425-2427 (2002).

[16] Konstantatos, G., Howard, I., Fischer, A., Hoogland, S., Clifford, J., Klem, E., Levina, L. & Sargent, E. H. Ultrasensitive solution-cast quantum dot photodetectors. *Nature* **442**, 180-183 (2006).

[17] Jin, Y., Wang, J., Sun, B., Blakesley, J. C. & Greenham, N. C. Solution-processed ultraviolet photodetectors based on colloidal ZnO nanoparticles. *Nano letters* **8**, 1649-1653 (2008).

[18] Chen, C. H., Chang, S. J., Chang, S. P., Li, M. J., Chen, I., Hsueh, T. J. & Hsu, C. L. Novel fabrication of UV photodetector based on ZnO nanowire/p-GaN heterojunction. *Chemical Physics Letters* **476**, 69-72 (2009).

[19] Bie, Y. Q., Liao, Z. M., Zhang, H. Z., Li, G. R., Ye, Y. *et al.* Self‐Powered, Ultrafast, Visible‐Blind UV Detection and Optical Logical Operation based on ZnO/GaN Nanoscale p‐n Junctions. *Advanced Materials* **23**, 649-653 (2011).

[20] Chen, X., Zhu, H., Cai, J. & Wu, Z. High-performance 4H-SiC-based ultraviolet pin photodetector. *Journal of applied physics* **102**, 024505-024505-024504 (2007).

[21] Monroy, E., Omnes, F. & Calle, F. Wide-bandgap semiconductor ultraviolet photodetectors. *Semiconductor science and technology* **18**, R33 (2003).

[22] Torvik, J. T., Pankove, J. I. & Van Zeghbroeck, B. J. Comparison of GaN and 6H-SiC pin photodetectors with excellent ultraviolet sensitivity and selectivity. *Electron Devices, IEEE Transactions on* **46**, 1326-1331 (1999).

[23] Dahal, R., Fan, Z., Lin, J. & Jiang, H. Hybrid AlN–SiC deep ultraviolet Schottky barrier photodetectors. *Applied Physics Letters* **90**, 263505-263505-263503 (2007).

[24] Burroughes, J., Bradley, D., Brown, A., Marks, R., Mackay, K., Friend, R., Burns, P. & Holmes, A. Light-emitting diodes based on conjugated polymers. *Nature* **347**, 539-541 (1990).

[25] Wöhrle, D. & Meissner, D. Organic solar cells. *Advanced Materials* **3**, 129-138 (1991).

[26] Katz, H. E., Bao, Z. & Gilat, S. L. Synthetic chemistry for ultrapure, processable, and high-mobility organic transistor semiconductors. *Accounts of Chemical Research* **34**, 359-369 (2001).

[27] Peumans, P., Yakimov, A. & Forrest, S. R. Small molecular weight organic thin-film photodetectors and solar cells. *Journal of applied physics* **93**, 3693-3723 (2003).

[28] Ray, D. & Narasimhan, K. High response organic visible-blind ultraviolet detector. *Applied Physics Letters* **91**, 093516 (2007).

[29] Carrano, J., Li, T., Grudowski, P., Eiting, C., Dupuis, R. & Campbell, J. High quantum efficiency metal-semiconductor-metal ultraviolet photodetectors fabricated on single-crystal GaN epitaxial layers. *Electronics Letters* **33**, 1980-1981 (1997).

[30] Sandvik, P., Brown, D., Fedison, J., Matocha, K. & Kretchmer, J. Dual-SiC photodiode devices for simultaneous two-band detection. *Journal of The Electrochemical Society* **152**, G199-G202 (2005).

[31] Xu, Z., Xu, C., Wang, Q., Jiang, W., Liu, C. *et al.* Highly efficient organic ultraviolet photodetectors based on a Cu (I) complex. *Synthetic Metals* **160**, 2260-2264 (2010).

[32] Kind, H., Yan, H., Messer, B., Law, M. & Yang, P. Nanowire ultraviolet photodetectors and optical switches. *Advanced Materials* **14**, 158 (2002).

[33] Ahn, S.-E., Ji, H. J., Kim, K., Kim, G. T., Bae, C. H., Park, S. M., Kim, Y.-K. & Ha, J. S. Origin of the slow photoresponse in an individual sol-gel synthesized ZnO nanowire. *Applied Physics Letters* **90**, 153106 (2007).

[34] Cheng, J., Zhang, Y. & Guo, R. ZnO microtube ultraviolet detectors. *J. Cryst. Growth* **310**, 57-61 (2008).

[35] Guo, F., Yang, B., Yuan, Y., Xiao, Z., Dong, Q., Bi, Y. & Huang, J. A nanocomposite ultraviolet photodetector based on interfacial trap-controlled charge injection. *Nature Nanotechnology* **7**, 798-802 (2012).

CHAPTER 3 ZnO/POLYMER NANOCOMPOSITE UV PHOTODETECTOR

3.1 Introduction

As described in chapter 2, the photodiode has low dark-current and fast response speed, but there is no gain. On the other hand, the photoconductor has large gain, but the dark-current is high too. In order to combine these two kinds of photodetectors to get both high gain and low dark-current, there must be a control layer in the photodetector to get the transition between photodiode and photoconductor. This control layer is described in Fig.3.1. This control layer must be sensitive to the incident light and can be used as the photo-switch. In the dark, the control layer is switched off and there is no charge injection; under illumination, it is switched on and the charge can be freely injected.

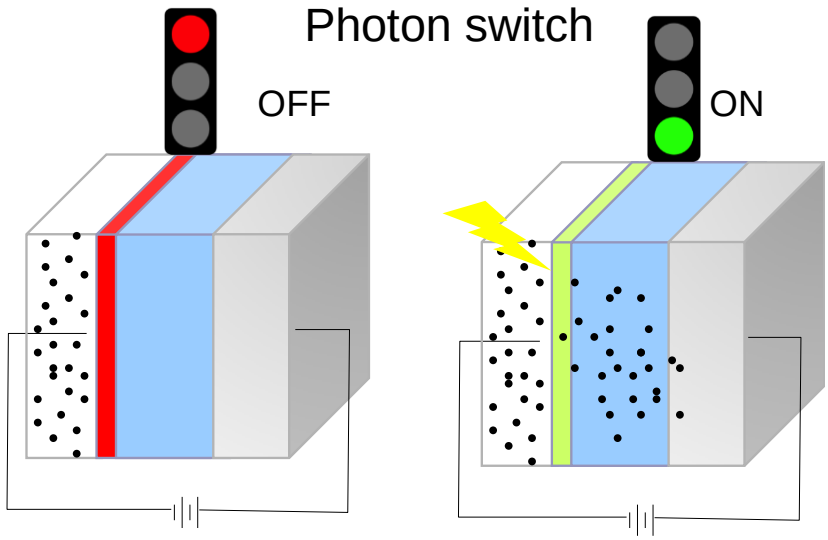

Figure 3. 1 Proposed control layer in a photodetector.

In this chapter, we are reporting on a new type of highly sensitive UV photodetector with a vertical device structure. The active layer materials are

nanocomposites composed of zinc oxide nanoparticles blended with semiconducting polymers [1], this layer also acts as the control layer.

ZnO nanostructure material is a potential alternative to GaN or SiC as an UV absorber due to its wide bandgap of ~3.4 electronvolt (eV), variable strategies and its low cost of material synthesis [2-10]. The nanocomposite UV photodetectors were fabricated by low-cost spin coating that is compatible with the complementary metal–oxide–semiconductor (CMOS) readout circuit [11]. As a result of interfacial trap-controlled charge injection, the photodetector transitions from a photodiode with a rectifying Schottky contact in the dark, to a photoconductor with an ohmic contact under illumination, and therefore combine the low dark current of a photodiode and the high responsivity of a photoconductor.

In the colloidal quantum dots (CQD) photoconductor reported elsewhere [5,12,13], the CQDs have two functions: trapping one type of charge and conducting the other types of charges. In the nanocomposite photoconductor here, the two functions are separated into two materials; and there is more flexibility to select/tune the material properties to meet different application requirements, such as response spectrum, response speed and detectivity. It should be noted that ZnO nanomaterials based UV-Photodetectors have been intensively explored in the past decade with most of the effort focusing on single nanowire(NW) for quick response due to the large carrier mobility in NWs [3,4,6-10,14,15]. However, these devices have not shown comparable performance or advantage to inorganic UV-Photodetectors for the following reasons: The detectors have been made of single

NW and then not scalable to large area with current synthesis techniques; ZnO NWs are connected to two electrodes directly leading to high dark-current. Based on the device structure and working principle reported here, our UV-Photodetectors are low-cost to made, easy to scale up to large area, and have very low dark-current, and then have great potential to replace the inorganic UV-Photodetectors.

3.2 Experimental Methods

3.2.1 Materials

The materials used in these nanocomposite UV photodetectors are summarized here. 2,9-dimethyl-4,7-diphenyl-1,10-phenanthroline (BCP) and polyvinylcarbazole (PVK) were purchased from SIGMA-ALDRICH; poly(3,4-ethylenedioxythiophene) poly(styrenesulfonate) (PEDOT:PSS) (PH4083) was purchased from H.C.STARCK; poly-3(hexylthiophene)(P3HT) was purchased from Rieke Metals. All materials were used as received without any purification. 4,4'-Bis[(p-trichlorosilylpropylphenyl)phenylamino]-biphenyl (TPD-Si_2) was synthesized following the route from literature [16,17]. To conclude, there are 3 steps in synthesizing TPD-Si_2.

Step 1: Synthesis of 4,4'-Bis[(p-bromophenyl)phenylamino)]biphenyl. To a toluene solution (50 mL) of tris(dibenzyldeneacetone)dipalladium (0.55 g, 0.60 mmol) and bis(diphenylphosphino)ferrocene (0.50 g, 0.90 mmol) was added 1,4-dibromobenzene (18.9 g, 0.0800 mol) at 25 ℃. After stirring under N_2 atmosphere for 10 min, sodium tert-butoxide (4.8 g, 0.050 mol) and

N,N‘-diphenylbenzidine (6.8 g, 0.020 mol) were added. The reaction mixture was then stirred at 90 ℃ for 12 h, followed by cooling to 25 ℃. The reaction mixture was then poured into water, and the organic and aqueous layers were separated. The aqueous layer was extracted with toluene (3 × 100 mL), and the resulting extracts were combined with the original organic layer. The solvent was removed in vacuum giving a crude product which was purified by chromatography on a silica gel column (6:1 hexane:ethylene chloride eluent) to yield pure 4,4‘-Bis[(p-bromophenyl)phenylamino)]biphenyl.

Step 2: Synthesis of 4,4‘-Bis[(p-allylphenyl)phenylamino]biphenyl. Using standard Schlenk techniques, 1.6 mL (3.5 mmol) of n-butyllithium(2.5 M in hexanes) was added dropwise under inert atmosphere to an ether solution (10 mL) of 4,4‘-Bis[(p-bromophenyl)phenylamino)]biphenyl (1.02 g, 1.58 mmol) while maintaining the temperature at 25 ℃. The mixture was stirred for 2 h, after that CuI (0.76 g, 4.0 mmol) was added. Upon cooling the reaction mixture to 0 ℃, allyl bromide (0.60 g, 5.0 mmol) was added in one portion, and the mixture was stirred for 14 h, followed by quenching with saturated aqueous NH_4Cl solution (100 mL) and extraction with ether (3 × 100 mL). The combined ether extracts were washed with water (2 × 100 mL) and brine (2 × 100 mL), and dried over anhydrous Na_2SO_4. Filtration and removal of solvent in vacuum afforded a yellow oil, which was further purified by chromatography on a silica gel column (4:1 hexane:methylene chloride) to yield 0.63 g of pure 4,4‘-Bis[(p-allylphenyl)phenylamino]biphenyl as a colorless solid.

Step 3: Synthesis of 4,4‘-Bis[(p-trichlorosilylpropylphenyl)phenylamino]biphenyl (TPD-Si_2). Under inert atmosphere at 25 ℃, a grain of H_2PtCl_6 ·nH_2O, followed by $HSiCl_3$ (0.73 g, 5.5 mmol), was added to a CH_2Cl_2 solution (30 mL) of 4,4‘-Bis[(p-allylphenyl)phenylamino]biphenyl (0.32 g, 0.55 mol), and the reaction mixture was stirred at 30 ℃ for 4 h. Removal of the solvent in vacuum yielded a dark-yellow oil, which was triturated with a mixture of 50 mL of pentane and 10 mL of toluene to yield a solid that was removed by filtration. The filtrate was concentrated in vacuum to yield TPD-Si_2.

Fig. 3.2 shows the chemical structures of the materials used in these devices.

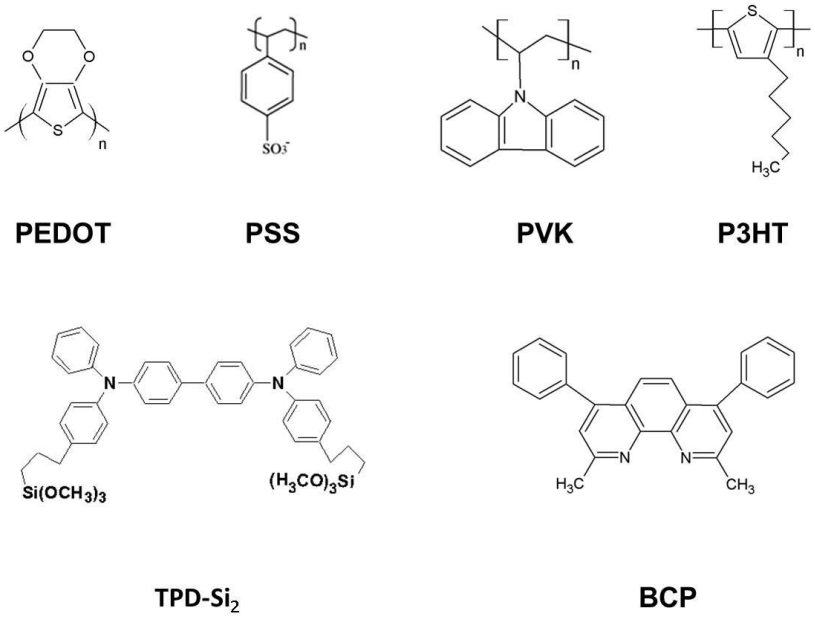

Figure 3. 2 Chemical structures of the materials used in the ZnO/Polymer nanocomposite UV photodetector.

3.2.2 Synthesis of ZnO Nanoparticles

ZnO nanoparticles were prepared by hydrolysis method in methanol by the following procedure [18,19]. In brief, 2.95 g (23mmol) $ZnAc_2.2H_2O$ was dissolved in

125 ml MeOH at 60℃ and followed by adding KOH solution (1.57 g KOH in 65 ml MeOH) within 5 minutes. After approximately 1.5 hour, the reaction solution turned from transparent to turbid, and the reaction mixture was stirred for one more hour. The small size nanoparticles were collected by centrifuge and were washed by methanol for three times, and then dispersed in chlorobenzene to form transparent solution. The average size of the ZnO nanoparticles made by this method is approximately 5~6 nm [20].

3.2.3 Device Structure and Fabrication

The designed device has a structure as shown in Fig.3.3. It has a vertical structure sandwiched between a transparent indium tin oxide (ITO) anode and an aluminum (Al) cathode. The active layer is a polymer layer blended with ZnO nanoparticles. Two types of hole-conducting semiconducting polymers were used for different response spectra: P3HT with a bandgap of 1.9 eV for UV-visible and PVK with a bandgap of 3.5 eV for UV detecting. This structure is essentially the same as that of the polymer/nanoparticle hybrid solar cells [21-23]. The difference is that the nanoparticles work as charge traps in our photodetectors in contrast to acting as a charge conductor in the hybrid solar cells. PVK is chosen because of its reasonably high carrier mobility and very high bandgap. In order to minimize the dark-current, a thin layer of blends of TPD-Si_2 and PVK with a thickness of 70 nm was inserted between PEDOT:PSS and the nanocomposite layer as the electron-blocking/hole-conducting layer. This blend of material combines the

hole-injection and hole-transport capabilities of TPD-Si_2 [17] with the electron-blocking capability of PVK and has been shown to reduce the dark-current by two to three orders of magnitude in our devices. On top of the active layer is the hole blocking/electron transporting layer of BCP with a thickness of 10 nm to further reduce the dark-curent.

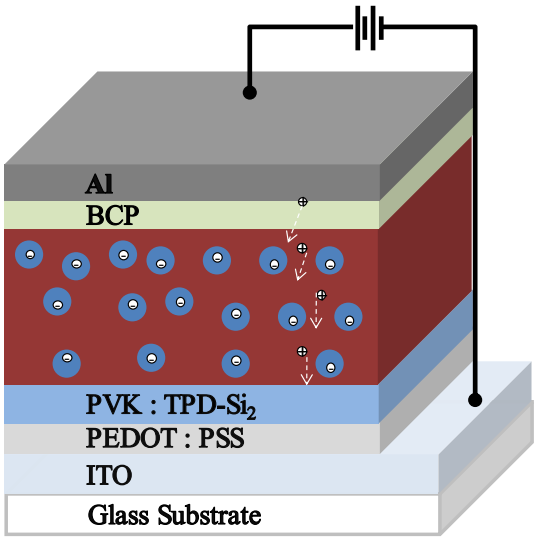

Figure 3. 3 Device Structure of the ZnO/polymer nanocomposite UV photetector.

For the device fabrication, PEDOT: PSS was first spin-coated onto a cleaned ITO glass substrate at a spin speed of 3,000 r.p.m., which gives a PEDOT: PSS film thickness of approximately 30 nm. The PEDOT:PSS was then baked at 120℃ for 30 minutes before spin-casting the polymer film. PVK was first dissolved in 1,2-dichlorobenzene (DCB) to make 20 mg/ml solution, followed by blending with TPD-Si_2 with a ratio of 1:1 by weight. TPD-Si_2 was a cross-linkable, hole-transporting organosiloxane material. The hole-transporting layer was obtained by spin-coating the blend at 4000 r.p.m. for 20 s, and the thickness of the blend film is approximately 70 nm. The film was then annealed at 100℃ for 1 hour in air to

crosslink TPD-Si_2 so that the photoactive layer coating that follows won't wash away this layer. The photoactive layers were made of blends of ZnO Nanoparticles with PVK or P3HT at the ratio of 3:1 by weight. The solutions were spin-coated at 1000 r.p.m. for 20 s, then solvent annealed for eight hours by placing the devices in the vapor of the solvent, which significantly slows down the drying of the polymers [24,25]. P3HT can form crystalline phase by the solvent-annealing which increases the hole mobility of the photoactive layer. The thicknesses of the active layers were approximately 500 nm. A BCP layer of approximately 10 nm was deposited by thermal evaporation onto the photoactive layer. To finish the device fabrication, a 100nm thick aluminum was thermally evaporated on the photoactive layer as the cathode. The active device area is 0.05 cm^2 which is defined by the shadow masks.

3.2.4 Device and Film Characterization

In this section, the device and film characterization are discussed, including the measurement of EQE, transient response, noise current, dynamic range, SEM, and EFM.

The external quantum efficiency was measured with the Newport QE measurement kit by focusing monochromatic beam of light onto the devices. The incident light was chopped at 35 Hz, and the optical power density is controlled to be less than 0.1mW/cm^2. A Si diode which has calibrated response from 280 nm to 1100 nm was used to calibrate the light intensity for photocurrent measurement.

For the transient response measurement, an optical chopper was used to get the light pulse of 800 Hz; a small resistor of 100 Ω was connected in series with the photodetector and a high speed and high sensitivity oscilloscope (Lecroy Wave Runner 104 Mxi-A, 1 GHz, 10 GS/s) was used to record the voltage across the resistor. The resistance of the device is above 45 kΩ under illumination. The small series resistance used won't perturb the circuit because it is much smaller than the resistance of the device. The absorption spectra of the photoactive layers of PVK:ZnO and P3HT:ZnO were measured with PerkinElmer Lambda 900 spectrometer. The film thickness of each layer was measured with an AMBIOS XP-2 stylus profilometer. All the measurements were carried out at room temperature in the ambient condition.

The noise current was directly measured with a Stanford Research SR830 Lock-In Amplifier using the method described by Konstantatos, G. *et al.* [11,12]. The devices were biased using alkaline batteries, and testing was carried out in an electrically shielded and optically sealed probe station, and on a floating table to minimize the vibrational noise. Through the choice of integration time, 1 s for our measurement, lock-in amplifier reported a noise current normalized to the measurement bandwidth in $A/Hz^{1/2}$.

The dynamic range was obtained by measuring the photocurrent under different light intensities. For light intensity below 1 μ W/cm^2, the monochromatic illumination was provided by a 350 nm LED with a PROTEK B8020FD function generator to supply a modulated bias to the LED. For higher light intensity up to 0.1

W/cm^2, the light was provided by Xe lamp with neutral density filters. The UV part of the light from Xe lamp is calculated by the integration of UV light intensity from Xe lamp spectrum. The photocurrents at different light intensities were recorded with a Lock-In Amplifier SR830 at a fixed frequency of 35 Hz. In both cases, the irradiance was calibrated with a Si diode at highest light intensity of each light source and Newport neutral density filters were used to modulate the light intensity from 0.1 W/cm^2 to 1 pW/cm^2.

The specific detectivities were calculated with the measured noise using the methods reported in reference [12]. The NEP was calculated by dividing the noise current by the responsivity under the same measurement frequency and bias. The specific detectivity D* was obtained as a function of wavelength, applied bias, and center frequency by dividing the square root of the optically active area of the device by the NEP.

The cross-section morphology of the P3HT:ZnO nanocomposite film was also measured by scanning electron microscopy (SEM). SEM was performed on a FEI Quanta 200 FEG SEM at high vacuum mode. The sample was prepared by cutting the P3HT:ZnO nanocomposite film on ITO glass substrate. In order to obtain a sharp cross-section, the ITO glass was firstly scratched by a glass cutter, and then the ITO glass, together with the nanocomposte film, was soaked in liquid nitrogen. The liquid nitrogen was used to provide a low temperature to the ITO glass. Therefore, the

scratched ITO glass and the nanocomposite film can be easily cut with sharp cross-section.

The electrostatic force microscopy (EFM) was used to characterize the topography and electron trap distribution in the nanocomposite films. EFM maps electric properties on a sample surface by measuring the electrostatic force between the surface and a biased AFM cantilever. EFM applies a voltage (+1 V in our measurement) between the tip and the sample, while the cantilever hovers above the surface without touching it. The cantilever deflects when it scans over static charges. The force arises from Coulomb interactions of the stored charge in ZnO nanoparticles, its image charges in the tip, and the induced charges due to the voltage EFM applied during imaging.

The absorption spectra of the photoactive layers of PVK:ZnO and P3HT:ZnO were measured with PerkinElmer Lambda 900 spectrometer. The film thickness was measured with AMBIOS XP-2 stylus profilometer. All the measurements were carried out at room temperature in the ambient condition.

3.3 Results and Discussion

In this part, we will discuss the working process of the photodetector, the performances of the photodetector, including the EQE, responsivity, specific detectivity, linear dynamic range, and response speed, etc. The photoconductive gain was also discussed.

3.3.1 Working Process of the Photodetector

The total working process of the photodetector can be summarized into 3 steps and is explained in Fig.3.3. Firstly, both the nanoparticles (NP) and polymers absorb incident photons and generate Frenkel excitons; Secondly, the Frenkel excitons diffuse to the polymer/nanoparticle interface and the electron transfer from the nanoparticles and semiconducting polymer, as shown in the energy diagram Fig.3.4 (a); Thirdly, holes transport in semiconducting polymer under the applied reverse bias/electric field, and electrons are still trapped in nanoparticles due to the lack of a percolation network for electrons and the strong quantum confinement effect in nanoparticles.

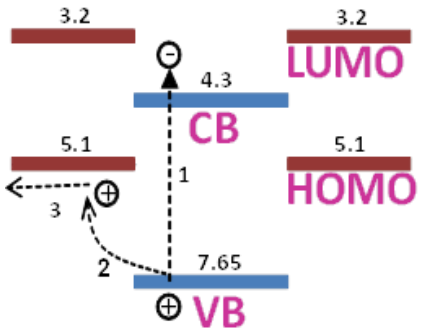

(a)

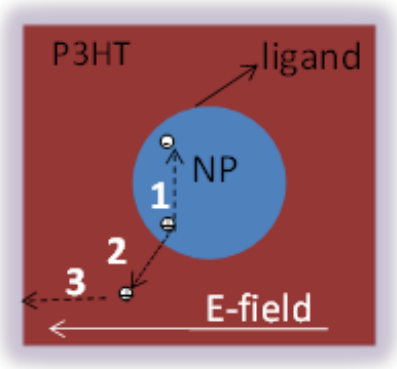

(b)

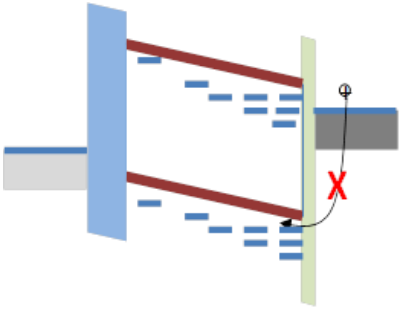

(c)

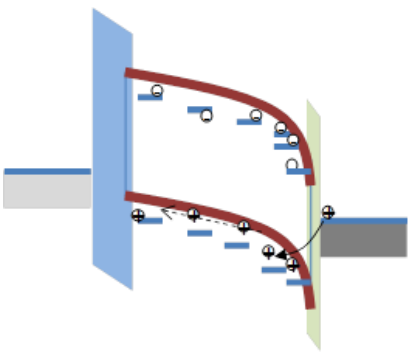

(d)

Figure 3.4 Working principle of the ZnO/polymer nanocomposite photodetector. (a). Energy diagram of the nanoparticle with the surrounding polymer. CB, conduction band; VB, valence band; LUMO, lowest unoccupied molecular orbital; HOMO, highest occupied molecular orbital. (b). Illustration of electron–hole pair generation (1), splitting (2), hole transport and electron trapping process. (c). Energy diagram of the device in the dark and under illumination (d). The device is reverse biased.

In the absence of illumination, the dark-current is small because of the very large charge injection barrier (>0.6 V) under reverse bias which is illustrated in Fig.3.3 (c); under illumination, the trapped electrons quickly shift the lowest unoccupied molecular orbital (LUMO) of the polymer downwards and align the Fermi energy of the Nanoparticles with that of the cathode.

The thickness of the hole-injection barrier on the cathode side becomes so small that the holes can easily tunnel through it at a small reverse bias, as shown in Fig.3.3 (d). Thus, the nanocomposite/Al interface acts as a photoelectronic "valve" for hole injection. Incident photons can switch on this "valve." The average energy barrier change, $\Delta\Phi$, is a linear function of trapped electron density (n_t), while the injection current follows an exponential relationship with the energy barrier change according to the Richardson-Dushman equation [26]:

$$J \propto \exp(-\frac{\Delta\Phi}{kT}) \propto \exp(\frac{n_t}{kT}) \tag{3.1}$$

where k is the Boltzmann constant and T is the temperature. The gain of a photodetector is the ratio of the measured photocurrent (carriers) versus the number of incident photons. If the injected hole number exceeds the absorbed photon number, there is gain due to the exponential dependence of injected holes on incident photons.

Since the polymer/cathode contact can supply sufficient hole current via injection (Ohmic contact) under radiation, holes are then efficiently injected into and circulate in the nanocomposite layer until they recombine with electrons. As long as the hole recombination lifetime is longer than the hole transit time through the nanocomposite layer, there is gain from the photoconductor phenomenon.

The electron traps are predominately close to cathode side because of the formation of vertical phase separation with ZnO nanoparticles segregated to cathode side, which was observed in P3HT:ZnO nanocomposite film with similar thickness and spin-coating process elsewhere [21]. Fig.3.5 shows the cross-section SEM of the nanocomposite film. A vertical composition profile is clearly observed: ZnO nanoparticles (bright color) prefer to stay close to the top surface while P3HT (dark color) is distributed close to the ITO substrate side.

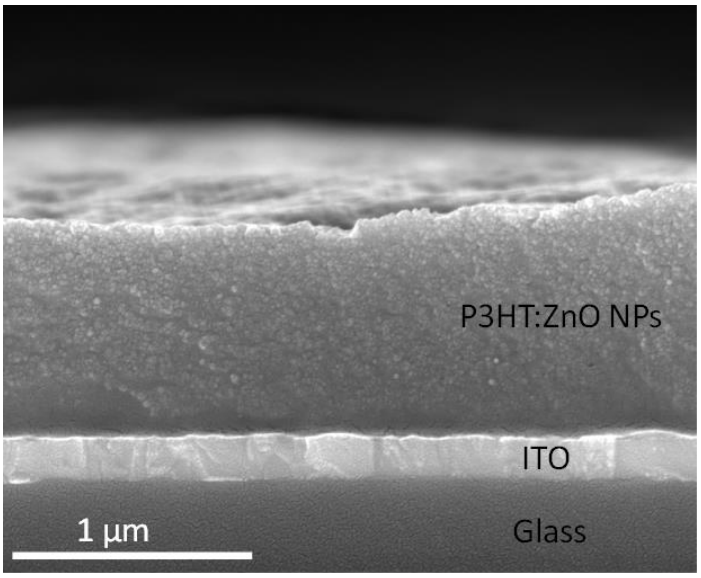

Figure 3. 5 Cross-section SEM of the P3HT:ZnO nanoparticles nanocomposite film on ITO glass substrate.

3.3.2 Verification of Electron Trapping in Active Layer

In order to verify the electron trapping in the nanocomposite layer, hole-only and electron-only devices have been made. The electron-only devices and hole-only devices have structures of ITO/Cs_2CO_3/P3HT:ZnO/Cs_2CO_3/Al and ITO/PEDOT:PSS/P3HT:ZnO/MoO_3/Al, respectively. The 1-3 nm thick Cs_2CO_3 layers formed by spin-coating or thermal evaporation result in a low work function surface so that only electrons can be injected [27]. Similarly, high-work-function interlayers such as PEDOT:PSS and MoO_3 guarantee hole injection only [28,29].

The current density in hole-only device is 3-4 orders of magnitude higher than electron-only device. This indicates that electrons can hardly move in the active layer due to the trapping of them by ZnO nanoparticles. On the other hand, holes can freely move with a relatively high mobility and thus enables the high photoconductive gain in our devices. Fig. 3.6 is J-V curve fitting for the electron-only and hole-only devices with the space charge limited current, respectively. The derived mobilities are 1.9 x 10^{-3} cm^2/V s for holes and 2.0 x 10^{-6} cm^2/V s for electrons in P3HT:ZnO film.

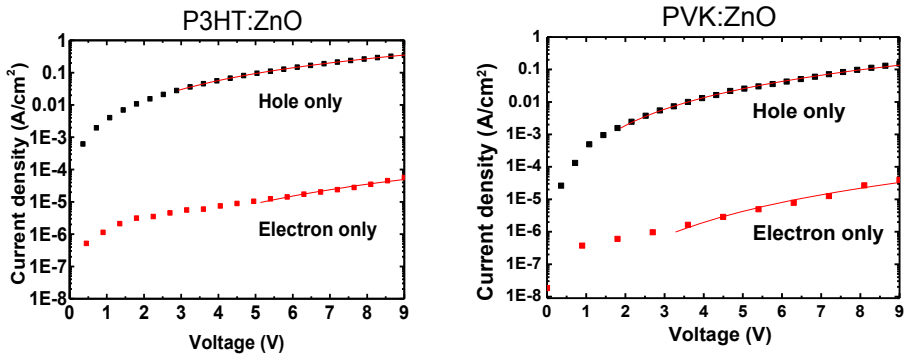

Figure 3. 6 J-V curve fitting of electron-only and hole-only devices of (a) P3HT:ZnO photodetector and (b)PVK:ZnO photodetector.

The electron trapping in active layer is also verified by the EFM measurement (Fig.3.7). The topography image shows a peak-valley difference of 20 nm which should be the size of ZnO NP aggregations. The nanocomposite surface was found to be covered by a high density of ZnO nanoparticles with a high coverage. The electrostatic force image agrees with the topography image very well. Larger electrostatic force between the ZnO nanoparticles and the tip (+1 V) was clearly observed which confirms the electron traps by the ZnO nanoparticles.

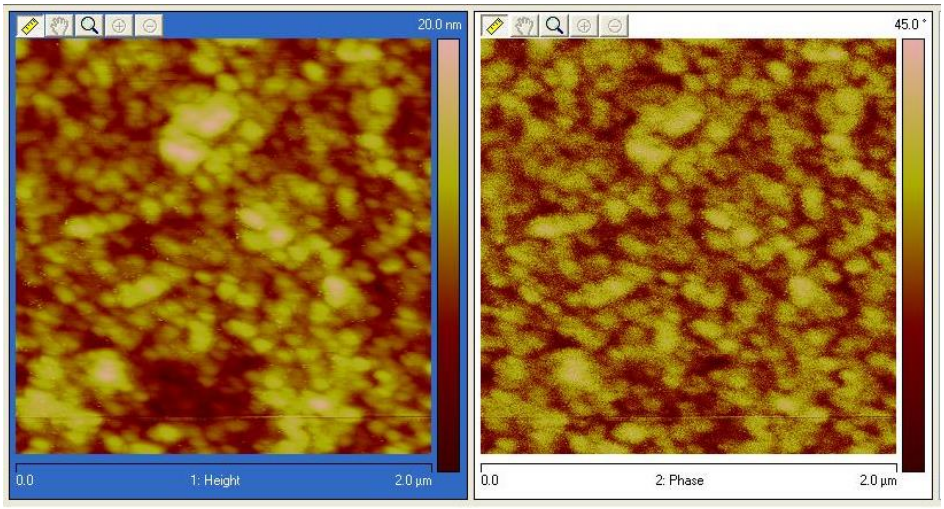

Figure 3. 7 EFM topography (a) and the electostatic force image (b) of the nanocomposite film. Scan size: 2 µm x 2 µm.

3.3.3 Performances of the Photodetector

To characterize the wavelength-dependent gain of the photodetectors, the dependence of the external quantum efficiencies (EQE) on wavelength were measured by the incident-photon-to-current efficiency (IPCE) system at different reverse bias; and the results are shown in Fig. 3.8 (a) and (b). The EQE curves agree with the absorption curves of the nanocomposites as well (Fig.3.9). The IQE (λ), which

characterizes the number of charges extracted out of the device per absorbed photon at each wavelength, can be calculated by IQE (λ) = EQE(λ)/abs. IQE measurement has been broadly used to characterize the charge extraction efficiency of photovoltaic cells, and IQE is generally less than 100% in photovoltaic cells. In our devices, IQE exceeds 100% at a bias of -3 V for ZnO:PVK devices and -1 V for ZnO:P3HT devices, respectively.

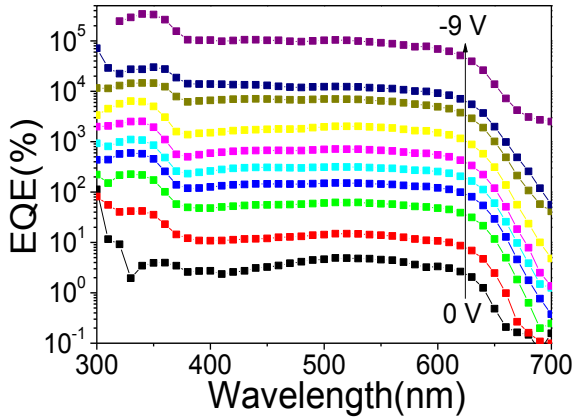

(a)

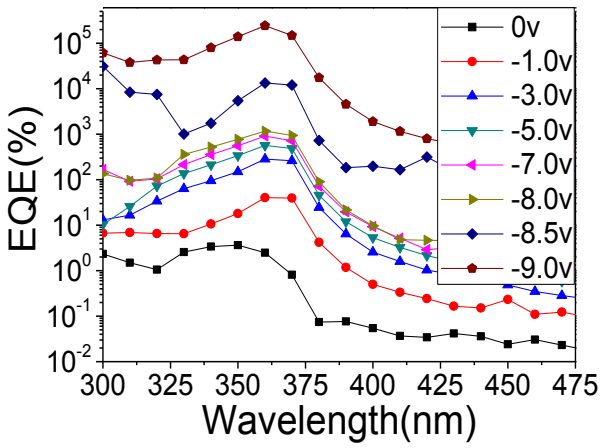

(b)

Figure 3. 8 External quantum efficiencies of (a). the P3HT:ZnO photodetector under reverse bias with a voltage step of 1 V and (b). the PVK:ZnO photodetector.

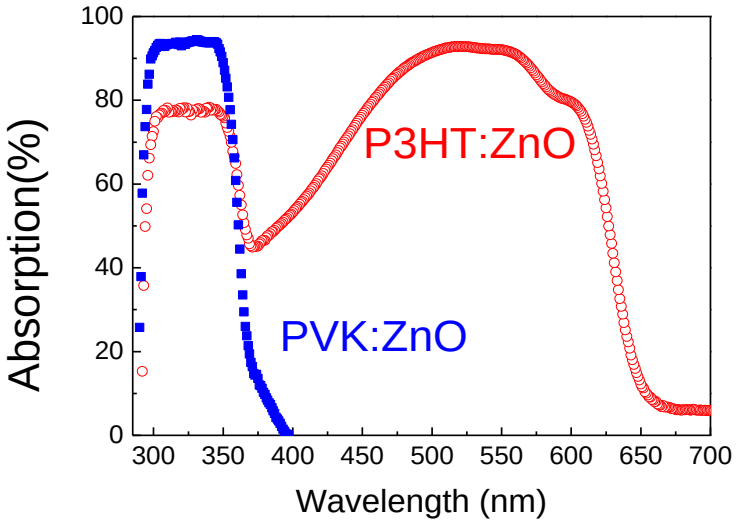

Figure 3. 9 The absorption spectra of the P3HT:ZnO and PVK:ZnO nanocomposite films.

There are four possible mechanisms where IQE can exceed 100% (or carrier multiplication): (1) multiple exciton generation (MEG) induced by quantum confinement [30] or single exciton fission [31], (2) impact ionization, (3) internal gain of the photoconductor and (4) multiple electron injection and collection per incident photon. The MEG effect does not apply to our devices because of the large bandgap ZnO nanoparticles and the absence of a triplet level in the middle of the polymers' bandgap. The impact ionization is not possible either due to the small applied bias, below 10 V. Therefore, the carrier multiplication must originate from the interface-controlled charge injection and photoconductive gain. And the high injection rate is prerequisite for the photoconductive gain.

EQEs increase quickly with increasing negative bias. The peak external quantum efficiency is 245,300% and 340,600% under bias of -9 V (the highest voltage output

of our lock-in amplifier) at 360 nm for the PVK:ZnO and P3HT:ZnO devices, respectively. The corresponding responsivity (*R* in A/W), i.e., the ratio of photocurrent to incident-light intensity, can be calculated from EQE with

$$R=EQE*e/h\nu \tag{3.2}$$

where *hv* is the energy of the incident photon in the electron-volt (eV). The peak responsivities, at illumination light intensity of 1.25 $\mu W/cm^2$, are 721 A/W for the PVK:ZnO device and 1001 A/W for the P3HT:ZnO device at 360 nm, which are more than three orders of magnitude larger than that of commercial GaN or SiC detectors (<0.2 A/W). These are the highest reported responsivities among all types of solid-state UV detectors [5,13,32]. A larger responsivity in the P3HT:ZnO device should be ascribed to the higher hole mobility of P3HT than that of PVK.

The gain of a photodetector is the ratio of the measured photocurrent carriers versus the number of the incident photons. There won't be any gain if it has Schottky contact, because the extracted charge number cannot exceed the absorbed photon number unless there are other processes such as avalanching, or quantum confinement-induced carrier multiplication. For our photodetector, the photocurrent shows a transition from injection limited to transported limited with the increased bias. Under a fixed incident light, the gain increases with applied bias. At low applied bias, for example, -1 V, the current flowing through the device is limited by carrier injection from the cathode. The gain is thus limited by the charge injection process which is determined by the electron trapping controlled hole injection. When the applied bias increases, the injection current quickly increase due to the narrowed hole

injection barrier. When cathode can supply enough holes at high reverse bias, the photocurrent flowing through the device is thus limited by the mobility of the holes of the low conductivity polymers. The device turns into a photoconductor at high bias, for example, at -9 V, with an ohmic contact formed. One can compare the magnitude of the forward and reverse biased photocurrent of the device to determine whether the device current is injection limited or transport limited. Under forward bias, the photocurrent through the device is transport limited because there is no or minimal charge injection barrier. It is clear that these devices turn into a photoconductor under illumination at high bias of -9 V, with an ohmic contact formed at cathode side.

The figure of merit for a photodetector is the specific detectivity which characterizes the capability of a photodetector to detect the weakest light signal [33]. In addition to the responsivity, the other factor that limits the specific detectivity of a detector is the noise current. The dark-current of these devices is as low as 6.8 nA at -9 V because of the blocking contact both at the anode and the cathode side in dark condition, as shown in Fig. 3.10, which gives a very low shot noise.

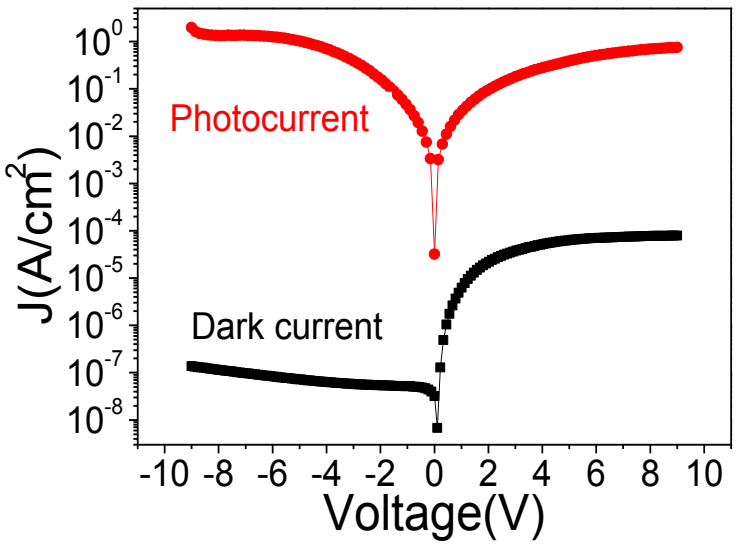

Figure 3. 10 Photocurrent and dark-current density of the PVK:ZnO photodetector.

As can be seen from Fig.3.10, there is a rapid increasing of the steady-state photocurrent at -9 V, which is consistent with the rapid increasing the measured external quantum efficiency values in both PVK:ZnO and P3HT:ZnO devices when the bias is above -8 V, as shown in Fig. 3.8. The current-voltage curve and the EQE curves are repeatable. The rapid increasing of photocurrent is not caused by device breakdown, because the dark-current density remains as low as approximately 135 nA/cm^2 after applying the -9 V bias. Actually, it takes about two minutes to finish one EQE measurement with the IPCE system. If the devices broke down at -9 V, the measured EQE curves wouldn't show any wavelength dependence. The EQE curves measured from 0 V to -9 V overlap with those measured from -9 V to 0 V. The EQE curves measured at -9 V overlap over 10 testing cycles, as shown in Fig.3.11.

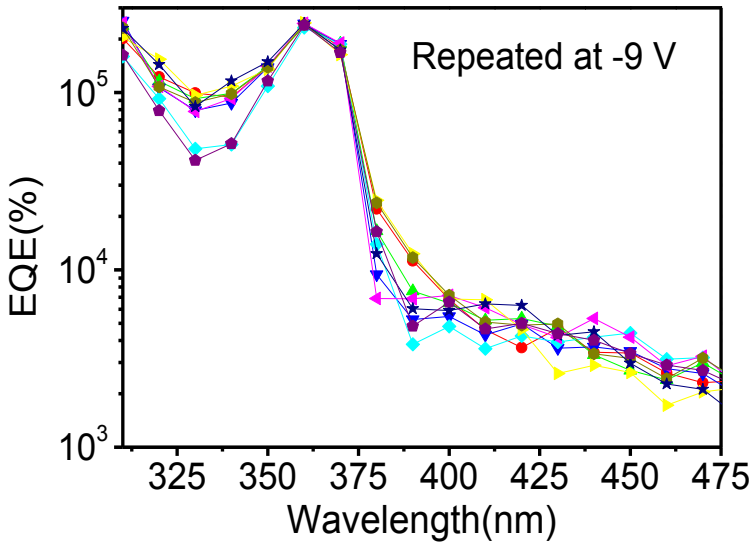

Figure 3. 11. Measured EQE of the PVK:ZnO photodetector at reverse bias of -9 V repeated for 10 times.

The shape increase of the photocurrent at -9 V may be caused by a transition of the hole current from shallow trap space charge limited current (ST-SCLC) to trap free space charge limited current (TF-SCLC) due to the filling of the traps by the large amount of injected holes at high applied bias. In both the ST-SCLC and TF-SCLC regions, the device current is in proportion to the square of the applied bias. While the ST-SCLC current is generally several orders of magnitude lower than the TF-SCLC current, there is a transition region from ST-SCLC to TF-SCLC where current increases superexponentially due to a rapid increase of free carrier concentrations at a higher voltage region [34,35]. In these device, the hole current before the abrupt increase region (0 V~-7 V) can be fitted by the ST-SCLC model very well. The sharp increase of current approximately -9 V is thus likely a behavior of the transition from ST-SCLC to TF-SCLC. Similar abrupt current increase has

been broadly reported in many other organic semiconductors, such as copper phthalocyanine (CuPc) film [36].

Noise current is an important parameter in determining the detectivity. To account for other possible noise, such as flicker noise and thermal noise, the total noise current of the photodetector was directly measured with a SR830 lock-in amplifier at different dark-current density and frequency [11,12]. As shown in Fig.3.12 (a) and (b), the measured total noise current was found to be dominated by the shot noise within the frequency range of 1 Hz to 5 kHz.

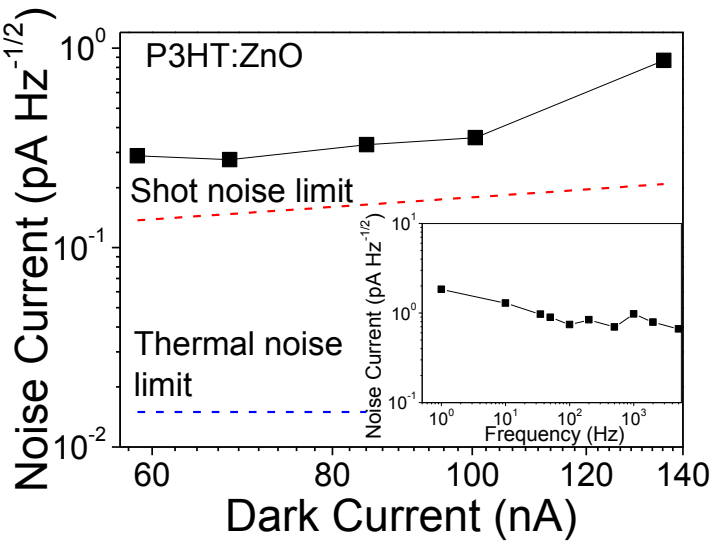

(a)

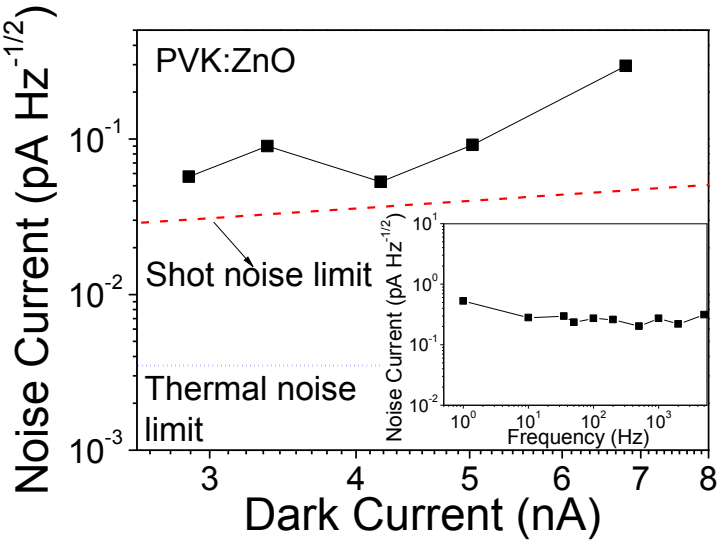

(b)

Figure 3. 12 Noise current of the P3HT:ZnO and PVK:ZnO photodetectors under different dark-currents. The insets show the frequency dependent noise current of the photodetector at -9 V.

The specific detectivities (D^*) of a photodetector are given by [33,37]:

$$D^* = \frac{(AB)^{1/2}}{NEP} \ (\text{cm Hz}^{\frac{1}{2}}\,\text{W}^{-1} \text{ or Jones}) \tag{3.3}$$

$$NEP = \frac{\overline{i_n^2}^{1/2}}{R} \ (W) \tag{3.4}$$

where A is the device area, B is the bandwidth, NEP is the noise equivalent power, $\overline{i_n^2}^{1/2}$ is the measured noise current, and R is the responsivity. The detectivities of our nanocomposite photodetector were calculated at different wavelengths with the measured noise current, responsivity at -9 V bias, and the results were plotted in Fig. 3.13. At illumination light intensity of 1.25 μW/cm^2, the specific detectivities at 360 nm are 3.4 × 10^{15} Jones for PVK:ZnO devices and 2.5 × 10^{14} Jones for P3HT:ZnO devices. The specific detectivities in the UV range are 2-3 orders of magnitude larger than silicon and GaN UV detectors. The specific detectivity of a P3HT:ZnO device

within the visible light range is also more than ten times better than that of silicon detectors.

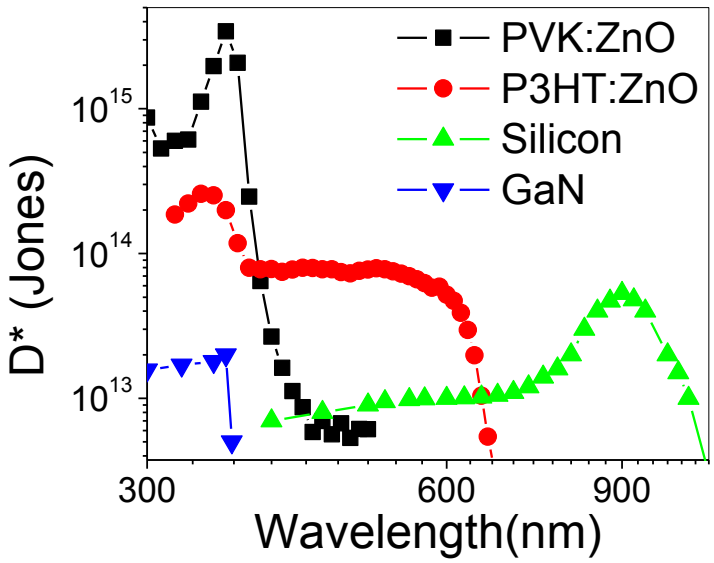

Figure 3. 13 Specific detectivities of the ZnO/polymer nanocomposite photodetector,Silicon and GaN photodetector at different wavelength.

These extremely high detectivities should be ascribed to the combination of the very high conductive gain and the low dark-current.

The other important parameter of photodetectors is the response speed. The temporal response of the nanocomposite detector was characterized by a chopper-generated short light pulse. Fig. 3.14 shows the transient photocurrent of the P3HT:ZnO device measured under a bias of -9 V at light intensity of 1 $\mu W/cm^2$. The transient response result shows a rise time (output signal to change from 10-90% of the peak output value) of 25 μs which was limited by the rising edge of the light pulse from the optical chopper. The decay of the photocurrent after switching off the UV

pulse has a fast component of 142 μs and a slow component of 558 μs, which indicates the existence of two channels for the recombination of holes. The response speed is the highest among all nanoparticles or colloidal quantum dot based photodetector [5,11-13,38]. The 3-dB bandwidth is 9.4 kHz. The devices provide over 10^5 fold improvement in gain-bandwidth product in solution-processed ZnO UV photodetection relative to previous reports [5]. The multiple-exponential decay time can be caused by the electron traps with different trap depths due to the non-uniform nature of ZnO nanoparticles or aggregates in the present hybrid devices. Deeper traps have longer charge release time and thus result in slower device response speed. It should be mentioned, that the photodetector response speed is related to the trap occupancy which depends on the light intensity. At the lower light intensity, the photocurrent decay is expected to be dominated by the slower process of 558 μs because deeper traps are easier to be filled. The response speed of the hybrid devices at light intensity lower than 1 $\mu W/cm^2$ has not been measured because a lower light intensity could not give enough photocurrent signals in the present measurement system.

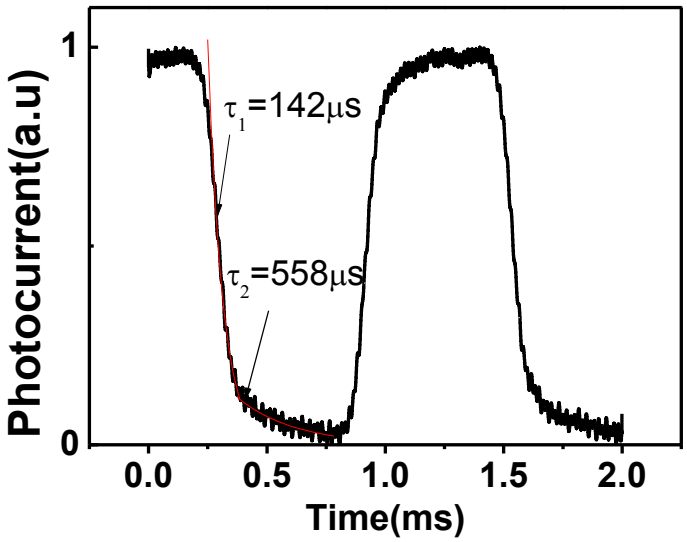

Figure 3. 14 Transient photo response waveform of a P3HT:ZnO detector with -9 V bias.

The photoconductive gain can be regarded as the ratio between electron recombination time, or device switch-off time, and the transit time that holes sweep through the nanocomposite film to the ITO. The calculated gain from the measured hole mobility and hole recombination time is 3,798 which is close to but slightly lower than the gain measured by the IPCE system. It can be understood that both mechanisms, interface controlled photomultiplication and photoconductor, contribute to the high gain. The difference between these two mechanisms is that the lifetime of the holes needs to be significantly larger than their transit time in a photoconductor, but the lifetime of the holes only needs to be slightly larger or equal to the transit time for an interface controlled photomultiplication device. The slightly high measured gain indicates that the interface-controlled charge photomultiplication also contributes which partially explains the high gain than other reported pure photoconductors.

A photodetector should have a large linear dynamic range to measure both strong and weak light. The linear dynamic range of the nanocomposite photodetector was also characterized by measuring the photocurrent at a fixed frequency of 35 Hz at varied light intensity from 10^{-1} W/cm^2 down to 10^{-12} W/cm^2. As shown in Fig. 3.15, the PVK:ZnO photodetector shows a linear response within the incident light intensity range from 10^{-1} to 10^{-9} W/cm^2, corresponding to an linear dynamic range of 80 dB. It is among the highest reported linear dynamic range for both inorganic and organic photodetector. The responsivity keeps almost constant in this light intensity range despite a slight (~10%) drop at high light level (inset of Fig. 3.15). This slight sublinear response at high light intensity is possibly caused by electron trapping saturation and/or limitation of hole mobility in the nanocomposite layers. The device begins to loss its linearity when the incident light intensity is below 10^{-9} W/cm^2. The responsivity drops to 52 A/W and the specific detectivity drops to 2.45×10^{14} Jones accordingly at a light intensity of 1.25×10^{-12} W/cm^2. The sub-linearity and declined detectivity at low light level is a disadvantage because high gain at low light intensity is desired for weak light detection, however, it can be improved by tuning the morphology of the nanocomposite layer. In principle, we expect a constant responsivity down to the lowest detectable incident light level (NEP) if the automatic transition from the Schottky junction to ohmic contact occurs at such a low incident light level. This is possible because the incident photons can cause a band bending in the local environment surrounding the light-absorbing ZnO nanoparticles which induces strong local hole injection. However, the degree of local band bending varies

with the morphology of the nanocomposite layer. If there is aggregation of ZnO nanoparticles, which is very likely to occur in our material system, the local average trapped electron density will be reduced and the induced charge injection will be weakened. In addition, there are still many ZnO nanoparticles located in the middle of nanocomposite layers or at the anode side despite the higher ZnO nanoparticles concentration at the cathode side due to the TPD-Si_2 interface-induced vertical phase separation. Light absorption by these ZnO nanoparticles far away from the cathode won't induce as much Schottky junction-narrowing effect as those close to the cathode side. This morphology is not ideal and might increase the lowest detectable light intensity of the nanocomposite photodetector. The influence of the morphology on the lowest detectable light intensity needs further investigation, and it is expected to see a lower limit of detectable light intensity and a better linear response by pushing more ZnO nanoparticles closer to the cathode side.

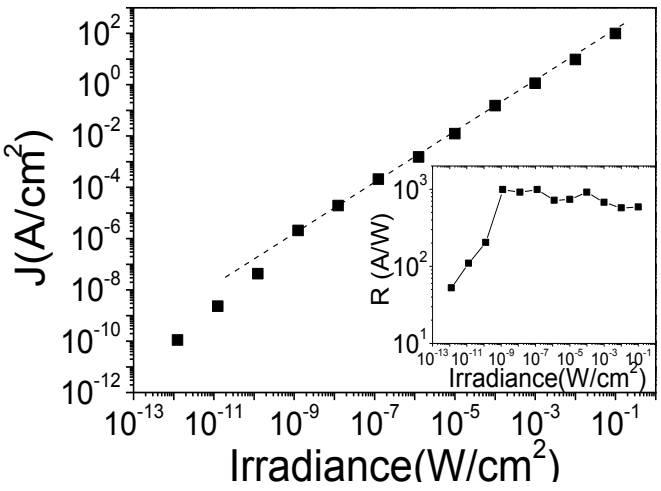

Figure 3. 15 Dynamic range of the PVK:ZnO photodetector; The inset shows responsivities under different illumination intensities.

The lifetime of a photodetector is also an important parameter [39-41]. Many applications require long term operation stability. However, they are all suffered from some degree of environmental and operational degradation, especially for the organic photodetectors [42,43]. The degradation can be due to the chemical or structural decomposition under high temperatures, strong radiation, humidity or oxygen. The degradation of our photodetectors in this dissertation has not been thoroughly studied yet and may need a further study in the future. Generally, device encapsulation is an effective way to improve the lifetime of the device [44]. More importantly, our photodetectors are designed for the ultra-weak light detection; therefore, they are expected to have longer lifetime than the detectors used for strong light detection.

3.3.4 Hole Mobility and Photoconductive Gain

For the case of trap-free or a discrete set of shallow traps space-charge limited current, the dependence of current and voltage obeys Child's law [45]:

$$J = \frac{9}{8}\varepsilon_r \varepsilon_0 \mu \frac{V^2}{d^3} \tag{3.5}$$

where ε_r is the relative dielectric constant, ε_0 is the permittivity of vacuum, μ is the effective charge carrier mobility, d is the organic layer thickness and V is the applied voltage.

Using ε_r = 3 for PVK and P3HT [46,47], d = 500 nm, V = 9 V, thus the hole mobility in the PVK:ZnO and P3HT:ZnO blend films can be determined using equation 3.5. The simulated hole mobility is 9.8×10^{-4} $cm^2/V\,s$ and 1.9×10^{-3}

$cm^2/V\ s$ for PVK:ZnO and P3HT:ZnO, respectively. The magnitude of these mobilities agrees well with many other reported [48-51].

Assuming the detector works in the pure photoconductor region, the photoconductor gain (G) can be calculated by the ratio of the recombination lifetime ($\tau_{lifetime}$) and transit time ($\tau_{transit}$) of the holes:

$$\left.\begin{aligned} G &= \tau_{lifetime} / \tau_{transit} \\ \tau_{transit} &= d / \mu_p E \\ E &= V / d \end{aligned}\right\} \qquad (3.6)$$

Where d is the inter electrode spacing, V is the applied bias, μ_p is the hole mobility and E is the electric filed. Using the hole recombination lifetime of 558 μs from the transit photo response measurement, V = 9 V, d = 500 nm, μ_p =1.9 $\times 10^{-3}$ cm^2/V s, the calculated photoconductor gain of P3HT:ZnO device is 3,798. It is very close to the measured gain by IPCE system.

3.4 Conclusions

To conclude, we reported a new type of hybrid photodetector based on ZnO nanoparticles/polymer nanocomposite materials, which is a diode in the dark and a photoconductor under illumination. Through the interfacial-trap controlled charge injection, they show tens to hundreds of times better detectivity than inorganic semiconductor photodetectors. These thin-film photodetectors have great potential for the existing applications in very weak UV and visible light detection and can

potentially open new application opportunities because of their flexibility, light weight and low cost.

3.5 References

[1] Guo, F., Yang, B., Yuan, Y., Xiao, Z., Dong, Q., Bi, Y. & Huang, J. A nanocomposite ultraviolet photodetector based on interfacial trap-controlled charge injection. *Nature Nanotechnology* **7**, 798-802 (2012).

[2] Chen, K. J., Hung, F. Y., Chang, S. J. & Young, S. J. Optoelectronic characteristics of UV photodetector based on ZnO nanowire thin films. *Journal of Alloys and Compounds* **479**, 674-677, doi:10.1016/j.jallcom.2009.01.026 (2009).

[3] Kind, H., Yan, H. Q., Messer, B., Law, M. & Yang, P. D. Nanowire ultraviolet photodetectors and optical switches. *Advanced Materials* **14**, 158-+ (2002).

[4] Soci, C., Zhang, A., Xiang, B., Dayeh, S. A., Aplin, D. P. R., Park, J., Bao, X. Y., Lo, Y. H. & Wang, D. ZnO nanowire UV photodetectors with high internal gain. *NANO LETTERS* **7**, 1003-1009, doi:10.1021/nl070111x (2007).

[5] Jin, Y. Z., Wang, J. P., Sun, B. Q., Blakesley, J. C. & Greenham, N. C. Solution-processed ultraviolet photodetedtors based on colloidal ZnO nanoparticles. *NANO LETTERS* **8**, 1649-1653, doi:10.1021/nl0803702 (2008).

[6] Liang, S., Sheng, H., Liu, Y., Huo, Z., Lu, Y. & Shen, H. ZnO Schottky ultraviolet photodetectors. *J. Cryst. Growth* **225**, 110-113 (2001).

[7] Lao, C. S., Park, M.-C., Kuang, Q., Deng, Y., Sood, A. K., Polla, D. L. & Wang, Z. L. Giant enhancement in UV response of ZnO nanobelts by polymer

surface-functionalization. *Journal of the American Chemical Society* **129**, 12096-+, doi:10.1021/ja075249w (2007).

[8] Basak, D., Amin, G., Mallik, B., Paul, G. K. & Sen, S. K. Photoconductive UV detectors on sol-gel-synthesized ZnO films. *J. Cryst. Growth* **256**, 73-77, doi:10.1016/s0022-0248(03)01304-6 (2003).

[9] Das, S. N., Moon, K.-J., Kar, J. P., Choi, J.-H., Xiong, J., Lee, T. I. & Myoung, J.-M. ZnO single nanowire-based UV detectors. *Applied Physics Letters* **97**, 022103 (2010).

[10] Li, Y., Della Valle, F., Simonnet, M., Yamada, I. & Delaunay, J.-J. High-performance UV detector made of ultra-long ZnO bridging nanowires. *Nanotechnology* **20**, 045501 (2009).

[11] Konstantatos, G., Clifford, J., Levina, L. & Sargent, E. H. Sensitive solution-processed visible-wavelength photodetectors. *Nature Photonics* **1**, 531-534, doi:10.1038/nphoton.2007.147 (2007).

[12] Konstantatos, G., Howard, I., Fischer, A., Hoogland, S., Clifford, J., Klem, E., Levina, L. & Sargent, E. H. Ultrasensitive solution-cast quantum dot photodetectors. *Nature* **442**, 180-183, doi:10.1038/nature04855 (2006).

[13] Konstantatos, G. & Sargent, E. H. Nanostructured materials for photon detection. *Nature Nanotechnology* **5**, 391-400, doi:10.1038/nnano.2010.78 (2010).

[14] Jin, Y., Wang, J., Sun, B., Blakesley, J. C. & Greenham, N. C. Solution-processed ultraviolet photodetectors based on colloidal ZnO nanoparticles. *Nano letters* **8**, 1649-1653 (2008).

[15] Chen, K.-J., Hung, F.-Y., Chang, S.-J. & Young, S.-J. Optoelectronic characteristics of UV photodetector based on ZnO nanowire thin films. *Journal of Alloys and Compounds* **479**, 674-677 (2009).

[16] Huang, Q., Li, J., Marks, T. J., Evmenenko, G. A. & Dutta, P. Triarylamine siloxane anode functionalization/hole injection layers in high efficiency/high luminance small-molecule green-and blue-emitting organic light-emitting diodes. *Journal of applied physics* **101**, 093101 (2007).

[17] Huang, Q., Evmenenko, G. A., Dutta, P., Lee, P., Armstrong, N. R. & Marks, T. J. Covalently bound hole-injecting nanostructures. Systematics of molecular architecture, thickness, saturation, and electron-blocking characteristics on organic light-emitting diode luminance, turn-on voltage, and quantum efficiency. *Journal of the American Chemical Society* **127**, 10227-10242 (2005).

[18] Liu, J., Qu, S., Zeng, X., Xu, Y., Gou, X., Wang, Z., Zhou, H. & Wang, Z. Fabrication of ZnO and its enhancement of charge injection and transport in hybrid organic/inorganic light emitting devices. *Applied surface science* **253**, 7506-7509 (2007).

[19] Pacholski, C., Kornowski, A. & Weller, H. Self-Assembly of ZnO: From Nanodots to Nanorods. *Angewandte Chemie International Edition* **41**, 1188-1191 (2002).

[20] Sun, B. & Sirringhaus, H. Solution-processed zinc oxide field-effect transistors based on self-assembly of colloidal nanorods. *Nano letters* **5**, 2408-2413 (2005).

[21] Oosterhout, S. D., Wienk, M. M., van Bavel, S. S., Thiedmann, R., Koster, L. J. A., Gilot, J., Loos, J., Schmidt, V. & Janssen, R. A. J. The effect of three-dimensional morphology on the efficiency of hybrid polymer solar cells. *Nature Materials* **8**, 818-824, doi:10.1038/nmat2533 (2009).

[22] Sun, B. Q., Marx, E. & Greenham, N. C. Photovoltaic devices using blends of branched CdSe nanoparticles and conjugated polymers. *NANO LETTERS* **3**, 961-963, doi:10.1021/nl0342895 (2003).

[23] Huynh, W. U., Dittmer, J. J. & Alivisatos, A. P. Hybrid nanorod-polymer solar cells. *Science* **295**, 2425-2427 (2002).

[24] Li, G., Shrotriya, V., Huang, J. S., Yao, Y., Moriarty, T., Emery, K. & Yang, Y. High-efficiency solution processable polymer photovoltaic cells by self-organization of polymer blends. *Nature Materials* **4**, 864-868 (2005).

[25] Li, G., Shrotriya, V., Yao, Y., Huang, J. S. & Yang, Y. Manipulating regioregular poly(3-hexylthiophene): 6,6 -phenyl-C-61-butyric acid methyl ester blends - route towards high efficiency polymer solar cells. *Journal of Materials Chemistry* **17**, 3126-3140 (2007).

[26] Modinos, A. in *Field, Thermionic, and Secondary Electron Emission Spectroscopy* 327-345 (Springer, 1984).

[27] Huang, J. S., Xu, Z. & Yang, Y. Low-work-function surface formed by solution-processed and thermally deposited nanoscale layers of cesium carbonate. *Advanced Functional Materials* **17**, 1966-1973 (2007).

[28] Kroger, M., Hamwi, S., Meyer, J., Riedl, T., Kowalsky, W. & Kahn, A. Role of the deep-lying electronic states of MoO 3 in the enhancement of hole-injection in organic thin films. *Applied Physics Letters* **95**, 123301-123301-123303 (2009).

[29] Gong, X., Moses, D., Heeger, A., Liu, S. & Jen, A.-Y. High-performance polymer light-emitting diodes fabricated with a polymer hole injection layer. *Applied Physics Letters* **83**, 183-185 (2003).

[30] Nozik, A. J., Beard, M. C., Luther, J. M., Law, M., Ellingson, R. J. & Johnson, J. C. Semiconductor Quantum Dots and Quantum Dot Arrays and Applications of Multiple Exciton Generation to Third-Generation Photovoltaic Solar Cells. *Chemical Reviews* **110**, 6873-6890, doi:10.1021/cr900289f (2010).

[31] Jadhav, P. J., Mohanty, A., Sussman, J., Lee, J. & Baldo, M. A. Singlet Exciton Fission in Nanostructured Organic Solar Cells. *NANO LETTERS* **11**, 1495-1498, doi:10.1021/nl104202j (2011).

[32] Sukhovatkin, V., Hinds, S., Brzozowski, L. & Sargent, E. H. Colloidal Quantum-Dot Photodetectors Exploiting Multiexciton Generation. *Science* **324**, 1542-1544, doi:10.1126/science.1173812 (2009).

[33] Liu, J.-M. *Photonic Devices, P 943*. (2005).

[34] Lampert, M. A. & Mark, P. *Current injection in solids*. (Academic Press New York, 1970).

[35] Takenobu, T., Bisri, S. Z., Takahashi, T., Yahiro, M., Adachi, C. & Iwasa, Y. High current density in light-emitting transistors of organic single crystals. *Physical Review Letters* **100**, 066601 (2008).

[36] Matsushima, T., Sasabe, H. & Adachi, C. Carrier injection and transport characteristics of copper phthalocyanine thin films under low to extremely high current densities. *Applied Physics Letters* **88**, 033508-033508-033503 (2006).

[37] Gong, X., Tong, M. H., Xia, Y. J., Cai, W. Z., Moon, J. S. *et al.* High-Detectivity Polymer Photodetectors with Spectral Response from 300 nm to 1450 nm. *Science* **325**, 1665-1667, doi:10.1126/science.1176706 (2009).

[38] Arnold, M. S., Zimmerman, J. D., Renshaw, C. K., Xu, X., Lunt, R. R., Austin, C. M. & Forrest, S. R. Broad Spectral Response Using Carbon Nanotube/Organic Semiconductor/C60 Photodetectors. *Nano Lett* **9**, 3354–3358 (2009).

[39] Li, N., Li, X., Demiguel, S., Zheng, X., Campbell, J. C. *et al.* High-saturation-current charge-compensated InGaAs-InP uni-traveling-carrier photodiode. *Photonics Technology Letters, IEEE* **16**, 864-866 (2004).

[40] Pernot, C., Hirano, A., Iwaya, M., Detchprohm, T., Amano, H. & Akasaki, I. Solar-blind UV photodetectors based on GaN/AlGaN pin photodiodes. *Japanese Journal of Applied Physics* **39**, L387 (2000).

[41] de Luna Bugallo, A., Tchernycheva, M., Jacopin, G., Rigutti, L., Julien, F. H., Chou, S.-T., Lin, Y.-T., Tseng, P.-H. & Tu, L.-W. Visible-blind photodetector based on p–i–n junction GaN nanowire ensembles. *Nanotechnology* **21**, 315201 (2010).

[42] Carrano, J., Li, T., Grudowski, P., Eiting, C., Dupuis, R. & Campbell, J. Comprehensive characterization of metal–semiconductor–metal ultraviolet photodetectors fabricated on single-crystal GaN. *Journal of applied physics* **83**, 6148-6160 (1998).

[43] Schuller, S., Schilinsky, P., Hauch, J. & Brabec, C. Determination of the degradation constant of bulk heterojunction solar cells by accelerated lifetime measurements. *Applied Physics A* **79**, 37-40 (2004).

[44] Carley, L. R. (Google Patents, 2006).

[45] Lampert, M. A. & Mark, P. Current injection in solids. (1970).

[46] Pfister, G. Hopping transport in a molecularly doped organic polymer. *Physical Review B* **16**, 3676 (1977).

[47] Ju ka, G., Genevi ius, K., sterbacka, R., Arlauskas, K., Kreouzis, T., Bradley, D. & Stubb, H. Initial transport of photogenerated charge carriers in π-conjugated polymers. *Physical Review B* **67**, 081201 (2003).

[48] Pandey, S. S., Takashima, W., Nagamatsu, S., Endo, T., Rikukawa, M. & Kaneto, K. Regioregularity vs regiorandomness: effect on photocarrier transport in Poly (3-hexylthiophene). *JAPANESE JOURNAL OF APPLIED PHYSICS PART 2 LETTERS* **39**, 94-97 (2000).

[49] Choulis, S., Kim, Y., Nelson, J., Bradley, D., Giles, M., Shkunov, M. & McCulloch, I. High ambipolar and balanced carrier mobility in regioregular poly (3-hexylthiophene). *Applied physics letters* **85**, 3890 (2004).

[50] DeLongchamp, D. M., Vogel, B. M., Jung, Y., Gurau, M. C., Richter, C. A. *et al.* Variations in semiconducting polymer microstructure and hole mobility with spin-coating speed. *Chemistry of materials* **17**, 5610-5612 (2005).

[51] Bao, Z., Dodabalapur, A. & Lovinger, A. J. Soluble and processable regioregular poly (3-hexylthiophene) for thin film field effect transistor applications with high mobility. *Applied Physics Letters* **69**, 4108 (1996).

CHAPTER 4 FULLERENE PHOTODETECTORS WITH WIDE LINEAR DYNAMIC RANGE

4.1 Introduction

Fullerene is one of the most widely studied materials for photovoltaic devices. The fullerene-based photodetector can works in both photoconductive mode and photovoltaic mode. In the photoconductive mode, the two electrode contacts are both Ohmic, and thus has a possibility with a gain higher than 1. If one kind of charge carriers were trapped by the active layer, another kind of carriers can be freely injected and transported throughout the device. In case of the transient time is shorter than the carrier lifetime, the photoconductive gain can exceed 1. Previous study showed that a fullerene photodetetor can has high EQE up to 5,000% [1]. However, this photodetector was suffered from the high dark-current. In this device, the noise current was found to be dominated by dark-current. Therefore, in order to detect weak light, the dark-current must be reduced.

The response characteristics, such as linearity, to very weak light are of ultimate importance when detectivity of photodetectors reaches the parity with traditional photodetectors [2-4]. Recent studies on organic photodetectors have focused on improving detectivity, but little attention was paid to the linearity of the organic photodetector's responsivity, especially in a low light intensity region [5-11]. The reported detectivities were mostly calculated according to the organic photodetector's

reponsivity at relatively strong light levels—orders of magnitude larger than the calculated noise equivalent power (NEP) [12]. It has not been shown yet whether the organic photodetectors can still maintain the high responsivity at low incident light intensity close to the NEP. However, there is concern that the organic photodetector would lose its high responsivity at such a low light level, beause there is generally a much higher density of charge traps in organic rather than inorganic semiconductor materials due to the amorphous or polycrystalline organic semiconductors used [13-15]. When the charge density generated by the incident light is comparable to the charge trap density, the photogenerated charges might be trapped rather than contribute to the device photocurrent.

In this chapter, we report on a highly sensitive, fullerene-based organic photodetector device which shows linear response from the indoor light intensity all the way down to 12 pW/m^2. This type of organic photodetector presents a linear dynamic range up to 90 dB [16].

4.2 Experimental Methods

4.2.1 Materials

C_{60} was purchased from Nano-C; BCP was purchased from SIGMA-ALDRICH; PEDOT:PSS was purchased from H.C.STARCK; All materials were used as received without any purification. TPD-Si_2 was synthesized following the route from literature [17,18], as described in chapter 3.

4.2.2 Device Design and Fabrication

Our aim is to fabricate a photodetector with very small noise current so that the small photocurrent generated with weak light can be distinguishable from the noise current. The light-absorbing material used in this study is fullerene (C_{60}) which is one of the most broadly studied materials for devices, including organic solar cells and organic field effect transistors, because of its excellent optoelectronic properties, such as a large light extinction coefficient, of 2.4×10^3 M^{-1} cm^{-1} at 480 nm[19], and high electron mobility, of up to 6-11 cm^2 V^{-1} s^{-1} [20-22]. In our organic photodetector devices here, the thickness of C_{60} is approximately 80 nm which allows more than 60% of the light above its optical bandgap to be absorbed. In previous study, it was found that C_{60} is a good photoconductor material with much longer hole trapping time than electron transit time. A photoconductive gain above 5,000% under reverse bias below -5 V has been observed in the device with a structure of indium tin oxide (ITO)/poly(3,4-ethylenedioxythiophene):poly(styrenesulfonate) (PEDOT:PSS) (35 nm)/ C_{60} (80 nm)/ 2,9-dimethyl-4,7-diphenyl-1,10-phenanthroline (BCP) (20 nm)/aluminum Al (100 nm) [23]. The high gain can be explained by the trapped-hole-enhanced electron-injection process: the photogenerated holes tend to be trapped at the interface of PEDOT:PSS and C_{60} layers, because C_{60} is a poor hole transport material. The high density trapped holes induce the band-bending in C_{60} at the interface of PEDOT:PSS and C_{60} layers. They also reduce the electron injection barrier dramatically, which eventually leads to strong secondary electron injection

from PEDOT:PSS to C_{60}. One trapped hole can induce the injection of more than one electron which generates the gain and such mechanism was also observed in another type of nanocomposite photodetector in previous study [23,24]. Despite of the high gain, these organic photodetector devices are not suitable for weak light detection because they suffer from high dark-current up to 2 mA/cm^2 at -6 V. Although there is a large electron injection barrier of 0.6 eV from PEDOT:PSS to C_{60} under reverse bias, the electron injection was enormously strong under reverse bias. This large dark-current might originate from the leakage current due to the thin, rough C_{60} layer and the broadening of the C_{60}'s lowest unoccupied molecule orbital (LUMO) of amorphous C_{60} film on the surface of PEDOT:PSS. Therefore increasing the thickness of C_{60} film won't be able to reduce the dark-current significantly. This strong electron injection provides the required Ohmic contact for the photoconductive gain but, on the other hand, results in large noise current. In addition, both the C_{60} and BCP layers are good electron transport materials, which help to conduct the large electron leakage current. Here, we try to reduce the dark-current by using a buffer layer of cross-linked 4,4'-Bis[(p-trichlorosilylpropylphenyl)phenylamino]-biphenyl (C-TPD) at the interface of PEDOT:PSS and C_{60}. The device structure of ITO/PEDOT:PSS (35 nm)/C-TPD (25 nm)/C_{60}(80 nm)/BCP (20 nm)/Al (100 nm) is shown in Fig. 4.1.

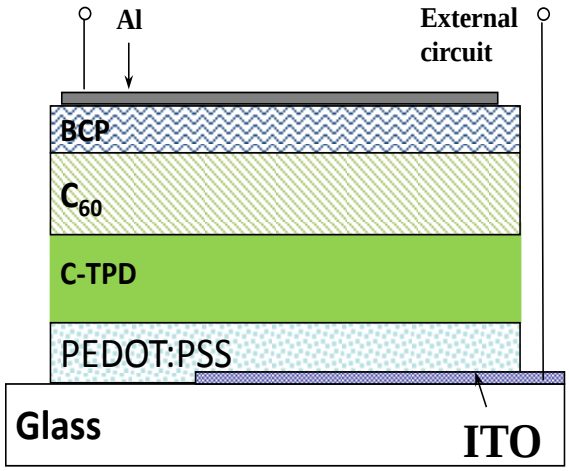

Figure 4. 1 Device structure of the fullerene photodetetor with C-TPD buffer layer.

For the device fabrication, PEDOT: PSS was first spin-coated onto a cleaned ITO glass substrate at a spin speed of 3,000 r.p.m., and then baked at 120 ℃ for 30 minutes; TPD-Si_2 was first spin coated on the top of a PEDOT:PSS layer and then thermally annealed at 110 ℃ for 1 hour in air to get it cross-linked; C_{60}, BCP and aluminum were deposited by thermal evaporation. The active device area is 0.05 cm^2 which is defined by the shadow masks.

The molecular structure and cross-linking process of the C-TPD layer is shown in Fig. 4.2, which is a thermal annealing-assisted hydrolysis process [25].

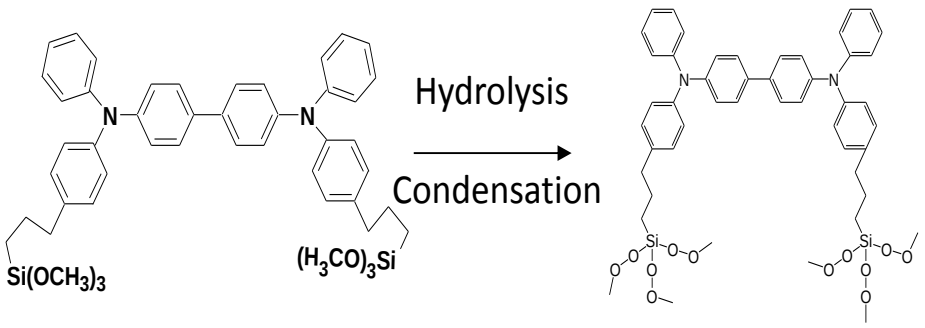

Figure 4. 2 The molecular structure and hydrolysis condensation process of C-TPD.

4.2.3 Device Characterization

For the device dynamic range measurement, different light sources were used to provide a large variation of light intensity by ten orders of magnitude. For light intensity below 1 μW/cm^2, the monochromatic light was provided by a 350 nm LED powered by a function generator. For stronger light intensity up to 0.1 W/cm^2, the light was provided by a Xe lamp; and the UV part of the light is calculated by the integration of UV light intensity from the Xe lamp spectrum. The light intensity was first calibrated with a Si diode at the highest light intensity of each light source, and the lower light intensities were obtained by attenuating the strong light with a set of Newport neutral density filters.

The shot noise limit is calculated by $i_{n,sh} = \sqrt{2eBi_d}$, where e is the elementary charge, B is the modulated bandwidth, i_d is the dark-current. The thermal noise limit is calculated by $i_{n,th} = \sqrt{\frac{4k_BTB}{R}}$, where k_B is Boltzmann constant, T is the absolute temperature, B is the modulated bandwidth, R is the resistance of the detector.

4.3 Results and Discussion

In this section, we will explain the working process of the photodetector, describe the performances of the photodetector, including the EQE, responsivity, specific detectivity, linear dynamic range, and response speed, etc. The results were also discussed.

4.3.1 Working Process

Fig.4.3 shows the energy diagram of the fullerene-based organic photodetector with C-TPD buffer layer. The device works under reverse bias, i.e. with negative bias applied to ITO eletctrode. In the dark, the electron injection barrier, i.e. the difference between the PEDOT:PSS work function and LUMO of C_{60}, is of the order of 0.6 eV. Few electrons can be injected at such a high electron injection barrier; furthermore, the C-TPD is a good electron blocking layer, which ensures a low dark-current. With illumination, the photogenerated excitons were firstly formed in the C_{60} bulk layer and then dissociated driven by the applied electrical field. Electrons drift to the Al electrode through BCP layer under reverse bias, and holes are transported to ITO electrode through C-TPD and PEDOT:PSS layer, thus forms the photocurrent.

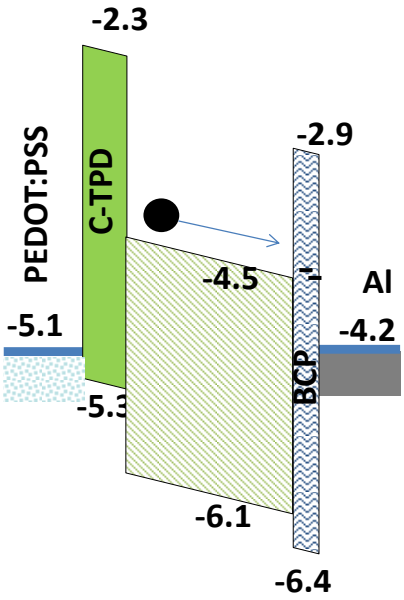

Figure 4. 3 The energy diagram of the fullerene-based organic photodetector with C-TPD buffer layer.

4.3.2 Performances of the Photodetector and Discussions

The measured EQE curves of the fullerene-based organic photodetectors with C-TPD buffer layer are shown in Fig. 4.4 (a) at different applied reverse bias. The highest EQE at -6 V is close to 40%. It is clear that there is no photoconductive gain with the insertion of a C-TPD layer compared with the photodetector without C-TPD layer (Fig.4.4 (b)). The inserted C-TPD layer interrupts the ohmic contact at the

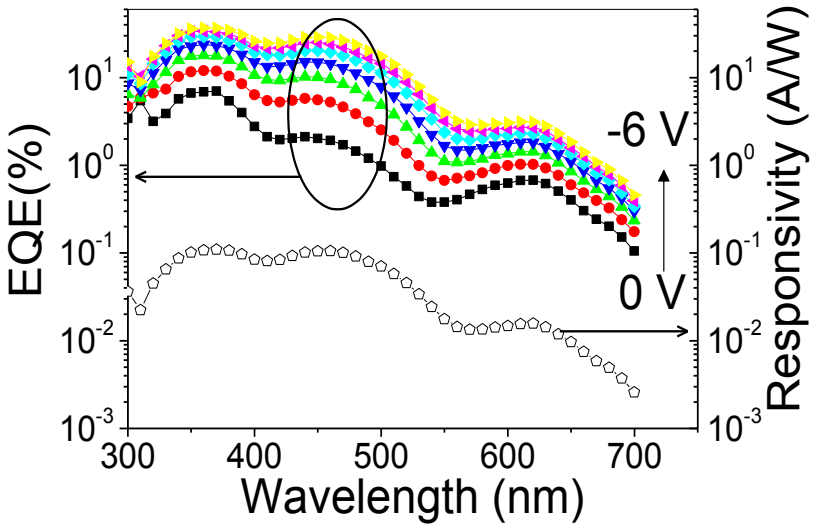

(a)

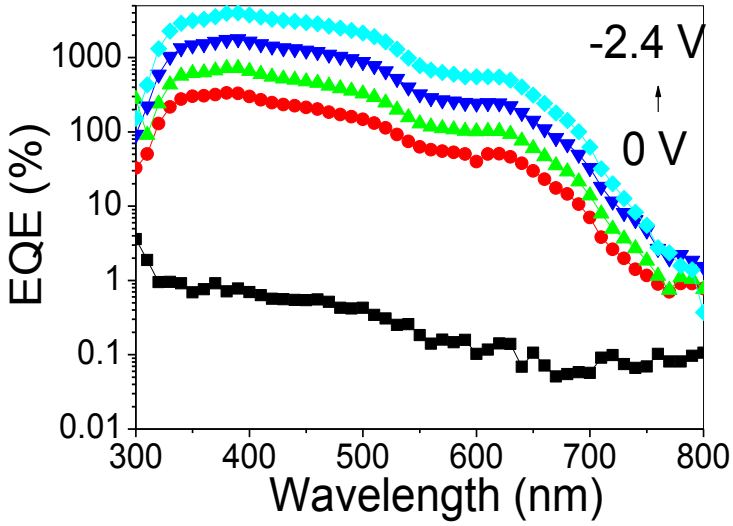

(b)

Figure 4. 4 (a) EQE/Responsivity of the fullerene photodetetor with C-TPD buffer layer and (b) EQE of the fullerene photodetector without C-TPD buffer layer.

PEDOT:PSS/C_{60} interface, as evident from the rectifying type dark-current curve shown in Fig.4.5. Therefore, there is no continuous supply of electrons for the photoconductive gain. From another prospective, the inserted C-TPD layer eliminates the trapped-hole-enhanced electron injection from PEDOT:PSS to C_{60} because C-TPD is too thick for the tunneling of electrons even though the hole can still be trapped in C_{60}.

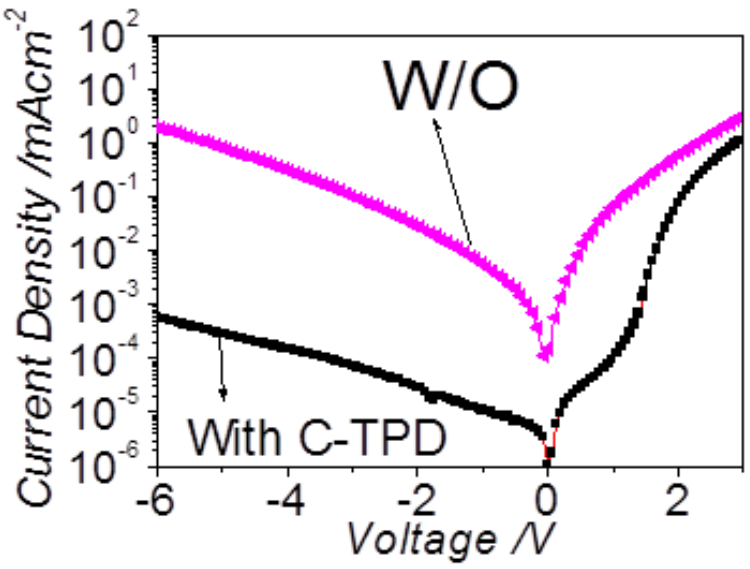

Figure 4. 5 Darkcurent density of the fullerene photodetectors with and without C-TPD buffer layer.

The lowest detectable light by a photodetector is characterized by NEP, which is the lowest light power needed to distinguish the photocurrent from noise current. The NEP of a photodetector can be described as [26]:

$$NEP = \frac{(2e\overline{i_b} + 2e\overline{i_d} + 4k_B T / R)^{1/2}}{\mathcal{R}} B^{1/2} \tag{4.1}$$

where e is the elementary charge, i_b is the photocurrent generated by background radiation, i_d is the the dark-current, k_B is the Boltzmann constant, T is the tempreture in kelvin, R is the resistance of the detector, B is the bandwidth, and $\mathcal{R}$ (the denominator in the equation) is the responsivity of the photodetector. For the photodetector working in UV-Vis regions, i_b can be neglected compared to the other two noise sources. Responsivity can be calculated from the measured external quantum efficiency by

$$R = EQE * e/h\nu \tag{4.2}$$

where *hv* is the energy of the incident photon. To find out the NEP for this type of organic photodetctors, the noise current was measured with a Stanford Research SR830 Lock-In amplifier following the method reported by G. Konstantatos *et al.* [27]. In order to be consistent with the EQE measurement, the lock-in frequency of the noise current was set to be 35 Hz, the same as the modulation frequency in the EQE measurement. Fig.4.6 shows the noise current vs. the dark-current. The shot noise limit and thermal noise limit calculated are also shown in the figure for comparison [26]. The measured noise current was found to be a little higher but very close to the shot noise limit. It is clear that the detector's noise was dominated by dark-current noise (shot noise). Therefore, in order to detect weak light, it is crucial to reduce the dark-current of organic photodetectors.

The insertion of this layer does increase the sensitivity of the fullerene-based organic photodetector yielding a much smaller NEP and larger specific detectivity due to the dramatically reduced noise current.

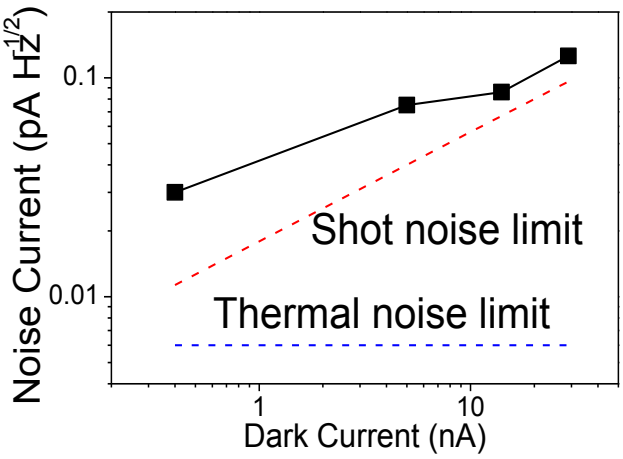

Figure 4. 6 The noise current of the fullerene photodetetor with C-TPD buffer layer.

The specific detectivity gives a fair comparison of different photodetectors by normalizing the device area [28,29]:

$$D^* = (AB)^{1/2} \mathcal{R} / i_n \ (Jones) \tag{4.3}$$

where A is the effective detector area in cm^2 , B is bandwidth, $\mathcal{R}$ is responsivity and i_n is the measured noise current. It can be seen that D^* is proportional to $\mathcal{R}$ and inversely proportional to the noise current. Although the responsivity of the C_{60} based photodetector was reduced by two orders of magnitude with the inserted C-TPD buffer layer compared to our previous photoconductive type C_{60} based photodetector, the dark-current was decreased by more than three orders of magnitude. Therefore the specific detectivity, or sensitivity of the C_{60} based photodetector, has been increased by 1 order of magnitude in this work. The peak D^* of the photodetector reaches 3.6 $\times 10^{11}$ Jones at 370 nm, as shown in Fig. 4.7, which is more than ten times higher than the control device without the C-TPD buffer layer.

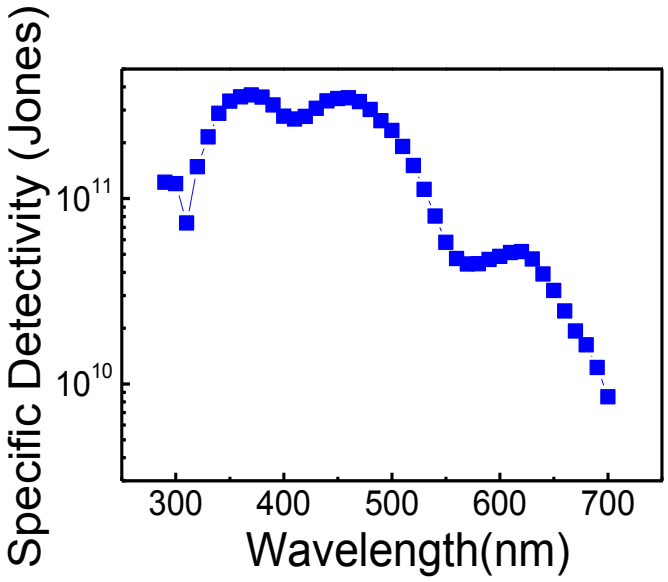

Figure 4. 7 The specific detectivity of the fullerene photodetetor with C-TPD buffer layer.

The upper limit of the fullerene-based organic photodetector response speed is limited by the electron transit time from the anode to the cathode side which is determined by the applied bias (V), thickness of the C_{60} film (*d*), and the mobility of electrons in C_{60}:

$$\tau_t = d^2 / \mu_e V \tag{4.4}$$

The calculated transit time is 1 ns under reverse bias of -6 V using a moderate electron mobility of 0.01 $cm^2V^{-1}s^{-1}$. The measured response time can be limited by the RC constant of the measurement circuit. The response speed was measured using a chopped light pulse recorded by an oscilloscope, as shown in Fig. 4.8. The RC time constant of the circuit is calculated to be 10~30 μs. And the shutter switching on (off) time is 50 μs, which is calculated from the spin-rate of the chopper. The device shows a rise and decay time of 50 μs which is clearly limited by the slow shutter switching on (off) speed. The response speed of the fullerene-based organic photodetector is quicker than 50 μs (20 kHz).

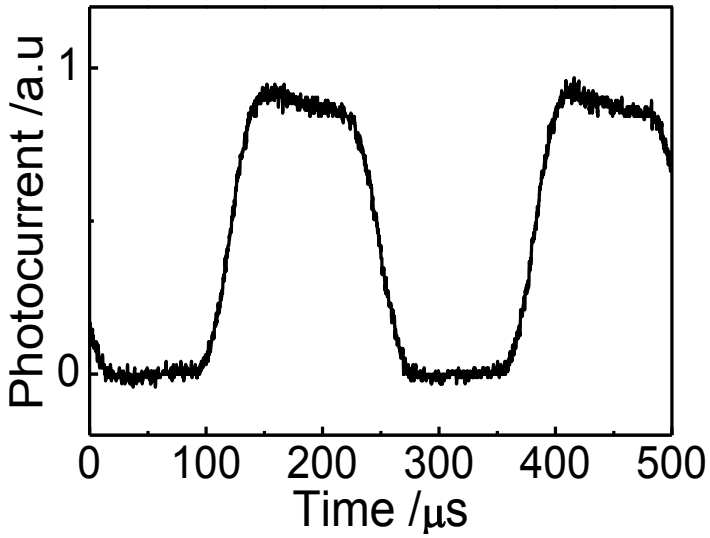

Figure 4. 8 Response speed of the fullerene photodetetor with C-TPD buffer layer.

As decribed above, the specific detectivity of our devices was calculated using the EQE measured at a relatively large incident light intensity of ~μW/cm^2. So direct comparison of specific detectivity might not tell the exact capability of a photodetector to detect the weak light with light intensity approaching NEP. In practical applications, a constant responsivity from strong light all the way down to weak light is critically important so that an organic photodetector can be applied for weak light sensing. Every photodetector only has a finite range of linear response and is characterized by linear dynamic range (LDR) in which the responsivity keeps constant. In inorganic photodetectors, LDR is limited by NEP at the weak light end and by saturation of photocurrent at the strong light end. But this senario does not necessarily hold for organic photodetectors because of the existing of large density of charge traps in most non-single crystal organic semiconductors. Here, the LDR of the fullerene-based organic photodetectors was directly measured by recording

photocurrent under modulated illuminations from strong light intensity of 0.1 W/cm^2 all the way down to NEP. The photocurrents of the fullerene organic photodetector device under different light intensities were recorded with a Lock-In Amplifier SR830 at a frequency of 35 Hz, and the result is shown in Fig. 4.9. The lowest detectable light intensity is 12 pW/ cm^2, with an effective device area of 0.05 cm^2, yielding a detectable power of 0.6 pW, which is very close to the calculated NEP of the C_{60} based photodetectors. This is the first time an organic photodetector with a linear response at such a low level light intensity has been reported. The photocurrent saturated at high light intensity reaches 0.1 W/cm^2. The fullerene organic photodetector device with a buffer layer has a linear response to varied light intensity by nine orders of magnitude, corresponding to a LDR of 90 dB. This high LDR is larger than those of many inorganic photodetectors, such as GaN (50 dB) [30] and InGaAs (66 dB) and approaches that of silicon photodetectors (120 dB) [28]. It is also among the highest reported LDRs for both small molecule and polymer-based organic photodetectors [8,28,31]. It is not clear yet why the fullerene-based organic photodetector has such a good linear response at such a low level of light, but it is expected that the following three factors should contributed to this large LDR observed in C_{60} based photodetectors here: 1) excellent electron transport property of fullerene [20-22]; 2) much more efficient free electron generation from Wannier exciton under small electric field in fullerene than any other organic semiconductor acceptor [32,33]; 3) the low density electron trap density in fullerene. The light intensity dependent of photocurrent was fitted by a line with a slope of 0.96. The

slightly deviation of the slope from 1 indicates there is still charge recombination in the photodetector. Since the photodetector device works under a high reverse bias of -6 V, it is expected that the bimolecular recombination, charge transfer exciton recombination or trap-assisted electron recombination should not dominate the recombination. While monomolecular recombination, such as Frenkel exciton recombination, is likely considering the relative thick C_{60} film of 80 nm and non-purified C_{60} used. It also indicates a path to future increase the performance of current C_{60} based photodetector by exploring the growth of highly crystalline C_{60} for higher speed, lower noise, and larger LDR organic photodetectors.

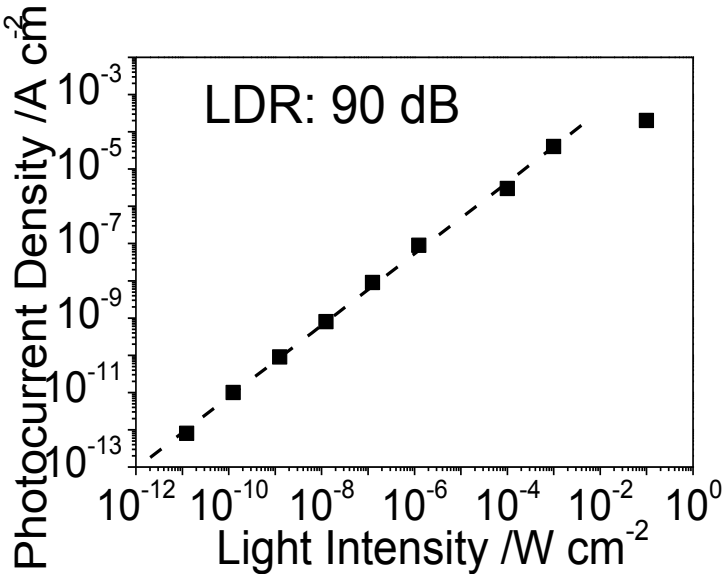

Figure 4. 9 Linear dynamic range of the fullerene photodetetor with C-TPD buffer layer.

4.3.3 Critical Role of C-TPD Layer

C-TPD has been studied in organic light-emitting diodes as an anode modification layer and hole injection/transport layer [18]. C-TPD is a good hole transport material, but it has poor electron mobility. This C-TPD layer introduces a

high electron injection barrier of 2.8 eV, which can greatly reduce the dark-current, as shown by the energy diagram in Fig. 4.2 [34,35]. The insertion of a C-TPD layer was found to reduce the dark-current density by three to four orders of magnitude compared with the control device without a buffer layer, as shown in Fig. 4.5.

In addition to increasing the electron injection barrier and suppressing electron transport, the cross-linked TPD at the ITO side is also expected to reduce the leakage current and eliminate catastrophic shorts by forming a condensed, smooth, conformal, and pin-hole free buffer layer on top of PEDOT:PSS [35]. In order to verify the role of this buffer layer in reducing the roughness of ITO and C_{60} layer, the surface roughness of each layer was measured with AFM. The stacking layer of ITO/PEDOT:PSS (35 nm)/C-TPD (25 nm)/C_{60}(80 nm) and the AFM images over the area of 2 μm × 2 μm are shown in Fig. 4.10. The commercial ITO is rough, with an average roughness of 4.547 nm. The spin-coated PEDOT:PSS layer can reduce the roughness of an ITO surface by almost three times; and the C-TPD layer can further reduce the roughness by four times, resulting in a very smooth surface with a roughness of 0.407 nm. A much smoother surface with a C-TPD buffer layer also improves the film quality of the C_{60} layer. As shown in Fig.4.10, the C_{60} layer on C-TPD is twice as smooth as the C_{60} layer on PEDOT:PSS. The more smooth and condensed C_{60} film should also contribute to the dramatically reduced small dark-current observed because of the reduced degree of disorder in C_{60}.

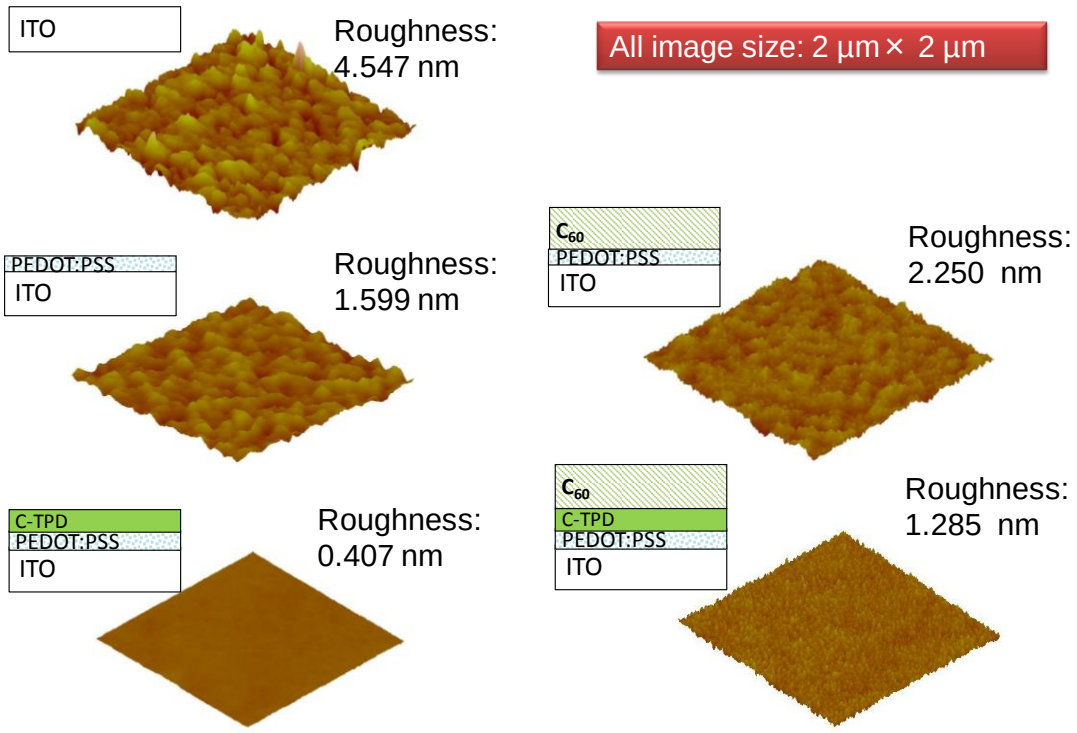

Figure 4. 10 AFM images of the surface with film stacking structure shown in the figure as well; Surface roughness is also labeled for each film surface.

The dark-current reduction in our devices should be due to the two factors: one is the introduced high electron injection barrier at the PEDOT:PSS/C-TPD interface, and the other is the reduced leakage current and catastrophic shorts due to the inserted compact C-TPD buffer layer and improved film quality of C_{60}. To find out which dominates the dark-current reduction, a series of devices were fabricated with different C-TPD thicknesses. In addition, a series of devices with a non-crosslinking polymer, polyvinylcarbazole (PVK) were also fabricated as the buffer layer. PVK was chosen here because it has comparable LUMO level with that of C-TPD, but does not has as good film forming capability as C-TPD. Therefore such comparison is

expected to distinguish the contribution of dark-current reduction from the two factors. Fig. 4.11 shows the dark-current of the devices at reverse bias of -6 V with different buffer layer thickness using C-TPD and PVK as buffer layers. It can be seen that inserting as thin as 15 nm C-TPD can reduce the dark-current of the C_{60} based photodetector by three orders of magnitude. Increasing the thickness of C-TPD up to 80 nm results in further reducing of the dark-current but by less than one order of magnitude. Although a thick C-TPD reduces the device dark-current, it also reduce the external quantun efficiency (EQE) and the device respond speed. All the device characteristis shown below are from the device with 25 nm C-TPD which gives a compromised combination of low noise and large external quantum efficiency and fast respond speed. The photodector devices using PVK buffer layer would have the same the dark-current with that with C-TPD buffer layer because of the introduced same energy barrier, if the dark-current reduction is solely caused by the introduced energy barrier. However, the dark-current of the devices with PVK buffer layer is two orders of magnitude higher than the device with C-TPD layers with same buffer layer thickness. Increasing the thickness of PVK is not effective to reduce the dark-current since 80 nm thick PVK doesn't give as low dark-current as 15 nm C-TPD. It is expected that the film quality of PVK is not good enough to exclude possible current leakage even when it is as thick as 80 nm. The results shown here indicate that although a large energy barrier can effectively reduce the charge injection and thus dark-current, a prerequisite is the film should be compact enough so that the leakage

current won't occur. It is thus concluded both factors contribute to the dark-current reduction in our devices and C-TPD combines these two very well.

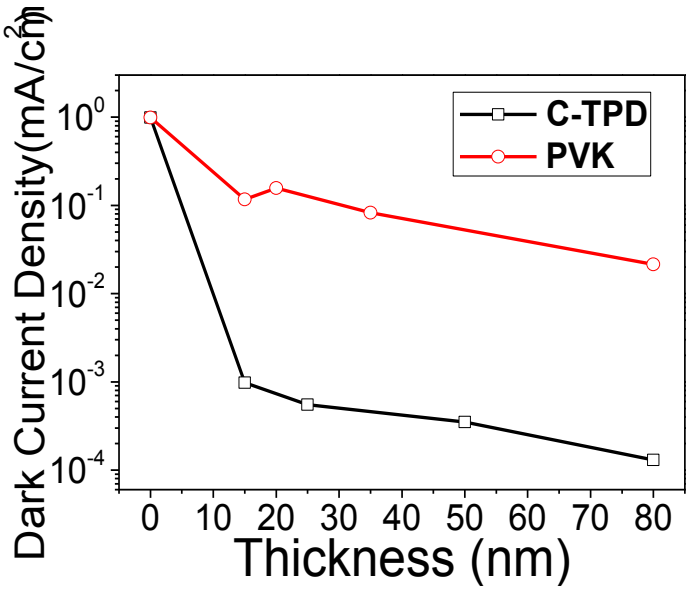

Figure 4. 11 Dark-current density of the fullerene-based photodetetors at the bias of -6 V using buffer layer of C-TPD and PVK of different thickness.

4.4 Conclusions

In summary, the dark-current of the fullerene UV photodetector has been successfully reduced by a C-TPD buffer layer. The high detectivity of 3.6×10^{11} Jones at 370 nm and the wide LDR of 90 dB, along with a response speed faster than 20 kHz, suggests that the fullerene-based organic photodetectors reported here can open the way for many potential applications, such as replacing the CCD array in a digital camera. The high sensitivity of this type of photodetector, particularly in the UV range, makes it potentially useful in monitoring the weak UV emission from scintillators which generally give UV emission.

4.5 References

[1] Huang, J. & Yang, Y. Origin of photomultiplication in C 60 based devices. *Applied Physics Letters* **91**, 203505-203505-203503 (2007).

[2] Klamkin, J., Ramaswamy, A., Johansson, L. A., Chou, H.-F., Sysak, M. N. *et al.* High output saturation and high-linearity uni-traveling-carrier waveguide photodiodes. *Photonics Technology Letters, IEEE* **19**, 149-151 (2007).

[3] Noorlag, D. & Middelhoek, S. Two-dimensional position-sensitive photodetector with high linearity made with standard IC-technology. *IEE Journal on Solid-State and Electron Devices* **3**, 75-82 (1979).

[4] Frehlich, R. G. Estimation of the nonlinearity of a photodetector. *Applied optics* **31**, 5926-5929 (1992).

[5] Peumans, P., Yakimov, A. & Forrest, S. R. Small molecular weight organic thin-film photodetectors and solar cells. *Journal of applied physics* **93**, 3693-3723 (2003).

[6] Clifford, J. P., Konstantatos, G., Johnston, K. W., Hoogland, S., Levina, L. & Sargent, E. H. Fast, sensitive and spectrally tuneable colloidal-quantum-dot photodetectors. *Nature Nanotechnology* **4**, 40-44 (2009).

[7] Zhou, Y., Wang, L., Wang, J., Pei, J. & Cao, Y. Highly Sensitive, Air‐Stable Photodetectors Based on Single Organic Sub‐micrometer Ribbons Self‐Assembled through Solution Processing. *Advanced Materials* **20**, 3745-3749 (2008).

[8] Konstantatos, G., Clifford, J., Levina, L. & Sargent, E. H. Sensitive solution-processed visible-wavelength photodetectors. *Nature Photonics* **1**, 531-534 (2007).

[9] Yu, G., Pakbaz, K. & Heeger, A. Semiconducting polymer diodes: Large size, low cost photodetectors with excellent visible - ultraviolet sensitivity. *Applied Physics Letters* **64**, 3422-3424 (1994).

[10] Ramuz, M., Bürgi, L., Winnewisser, C. & Seitz, P. High sensitivity organic photodiodes with low dark currents and increased lifetimes. *Organic Electronics* **9**, 369-376 (2008).

[11] Rauch, T., Böberl, M., Tedde, S. F., Fürst, J., Kovalenko, M. V., Hesser, G., Lemmer, U., Heiss, W. & Hayden, O. Near-infrared imaging with quantum-dot-sensitized organic photodiodes. *Nature Photonics* **3**, 332-336 (2009).

[12] Gong, X., Tong, M., Xia, Y., Cai, W., Moon, J. S. *et al.* High-detectivity polymer photodetectors with spectral response from 300 nm to 1450 nm. *Science* **325**, 1665-1667 (2009).

[13] Holmes, R., D'Andrade, B., Forrest, S., Ren, X., Li, J. & Thompson, M. Efficient, deep-blue organic electrophosphorescence by guest charge trapping. *Applied Physics Letters* **83**, 3818-3820 (2003).

[14] Podzorov, V., Menard, E., Borissov, A., Kiryukhin, V., Rogers, J. & Gershenson, M. Intrinsic charge transport on the surface of organic semiconductors. *Physical Review Letters* **93**, 086602 (2004).

[15] Kang, S. H., Crisp, T., Kymissis, I. & Bulović, V. Memory effect from charge trapping in layered organic structures. *Applied Physics Letters* **85**, 4666-4668 (2004).

[16] Guo, F., Xiao, Z. & Huang, J. Fullerene Photodetectors with a Linear Dynamic Range of 90 dB Enabled by a Cross‐Linkable Buffer Layer. *Advanced Optical Materials* **1**, 289-294 (2013).

[17] Huang, Q., Li, J., Marks, T. J., Evmenenko, G. A. & Dutta, P. Triarylamine siloxane anode functionalization/hole injection layers in high efficiency/high luminance small-molecule green-and blue-emitting organic light-emitting diodes. *Journal of applied physics* **101**, 093101-093101-093113 (2007).

[18] Huang, Q., Evmenenko, G. A., Dutta, P., Lee, P., Armstrong, N. R. & Marks, T. J. Covalently bound hole-injecting nanostructures. Systematics of molecular architecture, thickness, saturation, and electron-blocking characteristics on organic light-emitting diode luminance, turn-on voltage, and quantum efficiency. *Journal of the American Chemical Society* **127**, 10227-10242 (2005).

[19] Arbogast, J. W., Darmanyan, A. P., Foote, C. S., Diederich, F., Whetten, R., Rubin, Y., Alvarez, M. M. & Anz, S. J. Photophysical properties of sixty atom carbon molecule (C60). *The Journal of Physical Chemistry* **95**, 11-12 (1991).

[20] Li, H., Tee, B. C. K., Cha, J. J., Cui, Y., Chung, J. W., Lee, S. Y. & Bao, Z. High-Mobility Field-Effect Transistors from Large-Area Solution-Grown

Aligned C60 Single Crystals. *Journal of the American Chemical Society* **134**, 2760-2765, doi:10.1021/ja210430b (2012).

[21] Singh, T. B., Sariciftci, N. S., Yang, H., Yang, L., Plochberger, B. & Sitter, H. Correlation of crystalline and structural properties of C[sub 60] thin films grown at various temperature with charge carrier mobility. *Applied Physics Letters* **90**, 213512-213513 (2007).

[22] Bräuning, H., Trassl, R., Diehl, A., Theiß, A., Salzborn, E., Narits, A. A. & Presnyakov, L. P. Resonant Electron Transfer in Collisions between Two Fullerene Ions. *Physical Review Letters* **91**, 168301 (2003).

[23] Huang, J. & Yang, Y. Origin of photomultiplication in C60 based devices. *Applied physics letters* **91**, 203505 (2007).

[24] Guo, F., Yang, B., Yuan, Y., Xiao, Z., Dong, Q., Bi, Y. & Huang, J. A nanocomposite ultraviolet photodetector enabled by interfacial trap-controlled charge injection. *Nature Nanotechnology* **7**, 798-802 (2012).

[25] Cui, J., Huang, Q., Veinot, J. C. G., Yan, H., Wang, Q. *et al.* Anode interfacial engineering approaches to enhancing anode/hole transport layer interfacial stability and charge injection efficiency in organic light-emitting diodes. *Langmuir* **18**, 9958-9970 (2002).

[26] Liu, J.-M. 931-932 (Cambridge University Press, 2005).

[27] Konstantatos, G., Howard, I., Fischer, A., Hoogland, S., Clifford, J., Klem, E., Levina, L. & Sargent, E. H. Ultrasensitive solution-cast quantum dot photodetectors. *Nature* **442**, 180-183 (2006).

[28] Gong, X., Tong, M., Xia, Y., Cai, W., Moon, J. S. *et al.* High-detectivity polymer photodetectors with spectral response from 300 nm to 1450 nm. *Science* **325**, 1665-1667 (2009).

[29] Staveteig, P., Choi, Y., Labeyrie, G., Bigan, E. & Razeghi, M. Photoconductance measurements on InTlSb/InSb/GaAs grown by low‐pressure metalorganic chemical vapor deposition. *Applied Physics Letters* **64**, 460-462 (1994).

[30] Khan, M. A., Kuznia, J., Olson, D., Van Hove, J., Blasingame, M. & Reitz, L. High‐responsivity photoconductive ultraviolet sensors based on insulating single‐crystal GaN epilayers. *Applied Physics Letters* **60**, 2917-2919 (1992).

[31] Yu, G., Srdanov, G., Wang, J., Wang, H., Cao, Y. & Heeger, A. J. Large area, full-color, digital image sensors made with semiconducting polymers. *Synthetic metals* **111**, 133-137 (2000).

[32] Liu, T. & Troisi, A. What makes fullerene acceptors special as electron acceptors in organic solar cells and how to replace them. *Advanced Materials* **25**, 1038-1041 (2013).

[33] Yang, B., Guo, F., Yuan, Y., Xiao, Z., Lu, Y., Dong, Q. & Huang, J. Solution‐Processed Fullerene‐Based Organic Schottky Junction Devices for Large‐Open‐Circuit‐Voltage Organic Solar Cells. *Advanced Materials* **25**, 572-577 (2013).

[34] Im, W. B., Hwang, H. K., Lee, J. G., Han, K. & Kim, Y. Bright pure blue emission from multilayer organic electroluminescent device with purified unidentate organometallic complex. *Applied Physics Letters* **79**, 1387 (2001).

[35] Yan, H., Huang, Q., Cui, J., Veinot, J. G. C., Kern, M. M. & Marks, T. J. High‐Brightness Blue Light‐Emitting Polymer Diodes via Anode Modification Using a Self‐Assembled Monolayer. *Advanced Materials* **15**, 835-838 (2003).

CHAPTER 5 LARGE GAIN, LOW NOISE NANOCOMPOSITE ULTRAVIOLET PHOTODETECTORS

5.1 Introduction

In chapter 4, we introduced a cross-linkable buffer layer, 4,4'-Bis[(p-trichlorosilylpropylphenyl) phenylamino]-biphenyl (C-TPD), at the interface of PEDOT:PSS and C60 to reduce the dark-current. The pin-hole free and conformal C-TPD buffer layer dramatically reduced the dark-current density by 3-4 orders of magnitude. The significantly reduced dark-current enabled a constant responsivity from light intensity of 10^{-2} Wcm^{-2} all the way down to 12 $pWcm^{-2}$, resulting in a large linear dynamic range of 90 dB [1]. However, the insertion of 25 nm C-TPD between PEDOT:PSS and C60 interface also blocked the tunneling of electrons (secondary electron injection) into C60 even under large reverse bias of -6 V, and thus annulled the gain of C60 photodetectors.

Recent discovery of high gain in fullerene-based (C60) organic diode devices added the promise of organic photodetectors as potential candidates to replace inorganic counterparts [2,3]. It was demonstrated by us that a high gain above 50 from a C60 device with a structure of indium tin oxide (ITO)/poly(3,4-ethylenedioxythiophene):poly(styrenesulfonate) (PEDOT:PSS) (35 nm)/C60 (80 nm)/2,9-dimethyl-4,7-diphenyl-1,10-phenanthroline (BCP) (20 nm)/Al (100 nm) could be achieved under relatively low reverse bias of -4 V. The high gain

was proposed to be caused by an interfacial trap-controlled charge injection mechanism [2]. The trapped holes in the C60 close to PEDOT:PSS, excited by incident photons, reduce the energy barrier between the Fermi energy of PEDOT:PSS and LUMO of C60, and induced strong secondary electron injection under reverse bias. However, despite the large gain, the specific detectivity of such fullerene photodetectors was not high compared to inorganic UV photodetectors because of their relatively large dark-current. The disorder of n-type C60 causes the hole traps in it, which is the origin of the high gain, however brings in a relatively strong electron injection with a dark-current density of about 1 mA/cm^2 under reverse bias of -8 V [3].

In this chapter, we report on a fullerene-based photodetector with both large gain and low noise, enabled by the introduced C-TPD:ZnO nanocomposite buffer layer between the PEDOT:PSS and C60 layer. As a result, a record large linear dynamic range of 120 dB was achieved in these organic photodetectors which almost doubles that of the state-of-the-art commercial inorganic UV solid-state photodetectors [4].

5.2 Experimental Methods

5.2.1 Materials

C_{60} was purchased from Nano-C; BCP was purchased from SIGMA-ALDRICH; PEDOT:PSS was purchased from H.C.STARCK; All materials were used as received without any purification. TPD-Si_2 was synthesized following the route from literature [5,6], as described in chapter 3. ZnO nanoparticles were prepared using the same

method as in chapter 1, i.e., a hydrolysis method in methanol with some modifications [7,8].

5.2.1 Device Fabrication and Characterization

The device is fabricated by first spin-coating PEDOT:PSS onto a clean ITO glass substrate at a spin speed of 3000 rpm, and then baked at 120 ℃ for 30 min. Then a ZnO nanoparticles (5%, in 1,4-Dichlorobenzene solution) and TPD-Si_2 (2%, in Toluene solution) hybrid solution with the weight ratio of 1:1 was spin-coated onto the PEDOT:PSS layer and baked at 100 ℃ in the air for 60 min to get it cross-linked. After that, C_{60}, BCP and Al were sequentially evaporated onto the C-TPD:ZnO layer with the thickness of 80 nm, 10 nm, and 100 nm, respectively.

The UV-vis absorption spectra of the samples were measured by an Evolution 201 Spectrophotometer. The EQE was measured by a Newport Quantum Efficiency measurement kit with the incident monochromatic light to be modulated at the frequency of 35 Hz and the optical power density to be controlled at approximately 1 μWcm^{-2}. The capacitance verses frequency measurement was performed on an E4980A Precision LCR Meter, and the illumination of UV and green lights during the measurement were provided by a 365 nm laser diode and a 532 nm laser diode, with the light intensity of 30 $mWcm^{-2}$, respectively.

For the dynamic range measurement, different light sources with various light intensities were used. For the light intensity below 1 μWcm^{-2}, the monochromatic illumination was provided by a 350 nm LED with a function generator to supply the

modulated bias. For higher light intensity up to 0.1 Wcm^{-2}, Xe lamp was used. The UV part of the light from Xe lamp is calculated by the integration of UV light intensity from Xe lamp spectrum. The irradiance was first calibrated by a Si photodiode at the highest light intensity of each light source, and then attenuated by Newport neutral density filters.

5.3 Result and Discussions

Here, we will describe the working process of the photodetector, the performances of the photodetector, including the EQE, responsivity, specific detectivity, linear dynamic range, and response speed, etc. The results were also discussed.

The device structure of the photodetector is shown in Fig.5.1, which is composed of ITO (cathode)/PEDOT:PSS (35 nm)/C-TPD:ZnO (weight ratio 1:1) (30 nm)/C_{60} (80 nm)/BCP (10nm)/Al (anode) (100 nm). C_{60} was chosen as the photoactive material for its demonstrated high photoconductive gain and strong absorption in the ultraviolet–blue range [2]. Compared to our previously study in chapter 4 [1], ZnO nanoparticles were introduced into the C-TPD layer here. ZnO is a wide band gap semiconductor material, and also a potential alternative to GaN as the UV absorption material due to its merits of low cost and easy fabrication [9,10]. As shown in Fig.5.2, ZnO nanoparticles shows strong light absorption in the UV range, while the C_{60} layer's absorption spectrum covers a wide range from UV to blue-green region. As a result, the absorption of the device covers the UV-visible range. Besides the strong

UV absorption capacity, ZnO nanoparticles also possess large quantities of traps on the surface due to the large surface-to-volume ratio and hence high concentration of surface states. In chapter 3, we have demonstrated a ZnO/polymer hybrid UV photodetector with an extremely high gain of 3,406, which is based on the interfacial trap-controlled charge injection mechanism [11]. Inspired by that, it is expected that the ZnO nanoparticles in the C-TPD layer of the C_{60} photodetector may also behave as a photon-switchable valve to control the electron injection, and thus can recover its original high photoconductive gain.

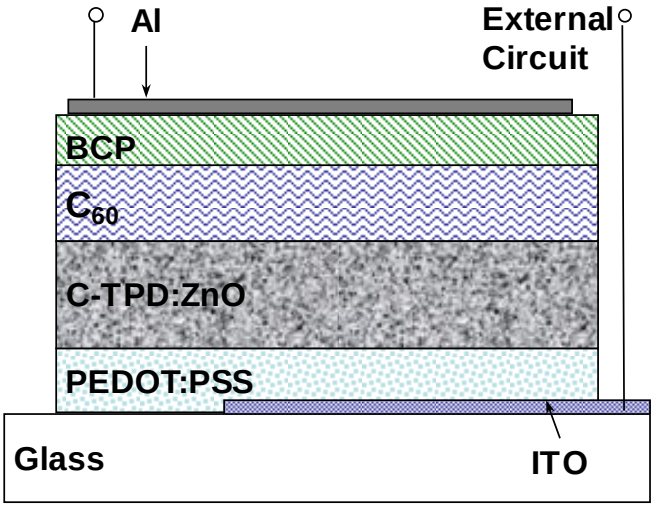

Figure 5. 1 Device structure of the large gain/low noise nanocomposite UV photodetector.

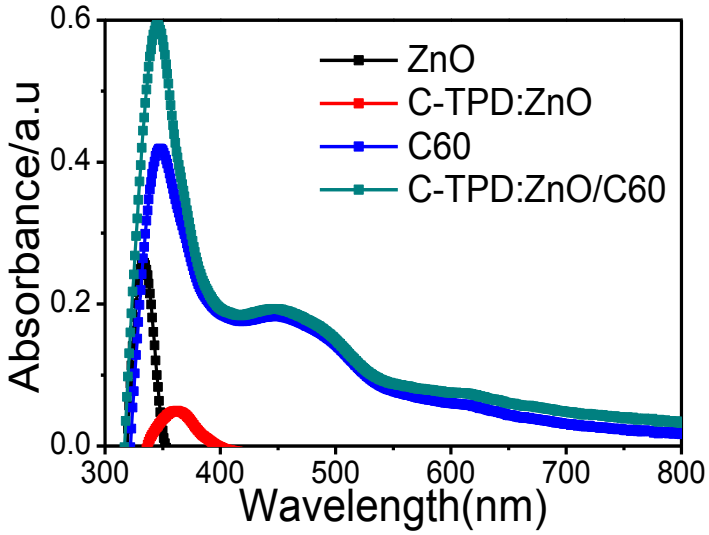

Figure 5. 2 The UV–vis absorption spectra of ZnO nanoparticle layer, C60 layer, C-TPD:ZnO layer, and C-TPD:ZnO/C60 double layer.

The device performance was firstly characterized by the external quantum efficiency (EQE) measurements. The measured EQE curves under different applied reverse biases are shown in Fig.5.3. The EQE values continuously increase throughout the UV-vis spectrum with the increase of the reverse bias. The peak values exceed 100% when the reverse bias is above -6 V, and further increase to 408% at 390 nm under the reverse bias of -8 V.

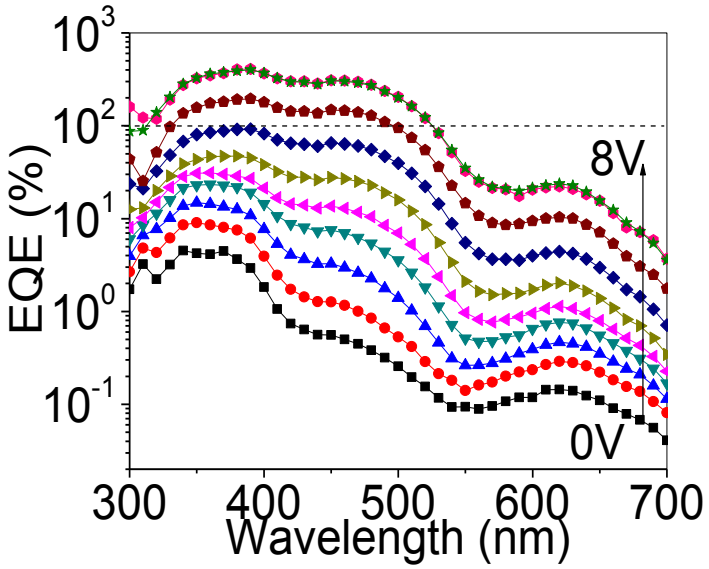

Figure 5. 3 EQEs of the photodetector under the reverse bias from 0 V to –8 V with a voltage step of 1 V.

The corresponding responsivity can be calculated from EQE by Eq.3.2. The peak responsivity is calculated to be 1.28 A/W at 390 nm, which is more than five times larger than those of commercial SiC and GaN UV detector (less than 0.2 A/W). This EQE value is also over one order of magnitude higher than the device without the ZnO nanoparticles in the C-TPD layer [1], which indicates the role of ZnO nanoparticles in inducing high gain in the device. The dark-current and photocurrent of the device are shown in Fig.5.4. It is found that the dark-current is comparable to our previous device without ZnO nanoparticles in the buffer layer, but a transition from a photodiode to a photoconductor occurs under illumination with the light intensity of 0.1 Wcm^{-2}, which leads to a large photocurrent. This means that the introduction of ZnO nanoparticles into the C-TPD buffer layer induces a large gain

while does not compromise the low dark-current of the detector, which is very beneficial to its light detection performance.

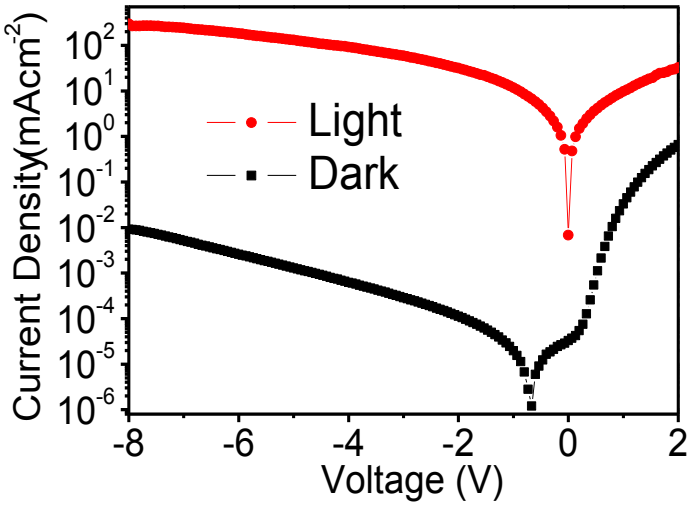

Figure 5. 4 Photocurrent density at light intensity of 0.1 Wcm^{-2} and dark-current density of the photoetctor.

The working principle of the photodetector can be understood by the energy band diagrams shown in Fig.5.5. It is shown that under reverse bias, when no ZnO nanoparticles are added into the C-TPD layer (Fig.5.5(a)), the electron injection from PEDOT:PSS to C_{60} is blocked by the C-TPD layer owing to its low electron mobility and the large electron injection barrier of about 2.8 eV. Therefore, the hole trap induced electron injection at the PEDOT:PSS/C_{60} interface is largely hampered under illumination, which results in the loss of gain of the device. For the device with C-TPD:ZnO nanocomposite as the buffer layer (Fig.5.5(b)), although ZnO is a good electron transport material, the large amount of surface states on the ZnO nanoparticles will induce the upward bending of the energy band [10]. It leads to the formation of low-conductivity depletion layer on the surface, and hence the energy

barrier between nanoparticles that obstructs the transportation of electrons through the buffer layer. Therefore, the low dark-current can still be maintained. In contrast, when light is illuminated onto the device, both the ZnO nanoparticles and C_{60} layer will absorb the incident light and generate excitons. The photo generated electrons and holes will move towards opposite directions under the applied reverse bias, with the electrons running towards the anode while the holes flowing to the C-TPD:ZnO layer. Due to the large quantities of hole-traps on the surface of ZnO nanoparticles, the photon-generated holes tend to be trapped by the ZnO nanoparticles instead of being collected by the cathode. The trapped holes then recombine with the electrons on the surface states, therefore alleviate the energy bending near the surface and reduce the width of the depletion layer. As a result, electrons can readily transport between ZnO nanoparticles under a small reverse bias. In this way, the electron transport between PEDOT:PSS and C_{60} is no longer blocked under illumination, thus the interfacial hole trap induced electron injection at the C_{60} layer is recovered, which leads to a high gain and large photocurrent.

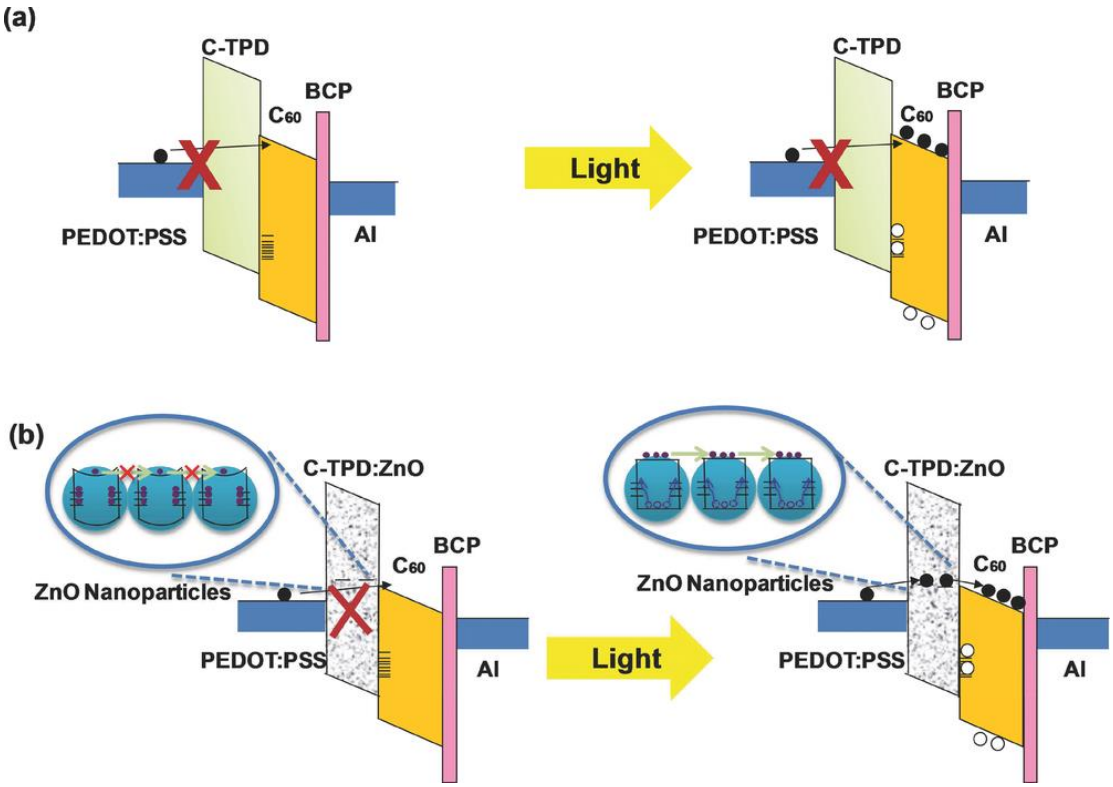

Figure 5. 5 Energy band diagrams of the reverse-biased photodetectors in the dark and under the illumination: (a) without and (b) with ZnO nanoparticles in the C-TPD buffer layer.

In order to verify the role played by the C-TPD:ZnO layer in the photodetector, the electron-only and hole-only devices were fabricated with the C-TPD:ZnO composite as the carrier transport layer. The corresponding J-V curves (Fig.5.6) exhibit that the electron current density is three to four orders of magnitude lower than the hole current density. This means that the C-TPD:ZnO layer is not a good electron transport material in the dark, so it can function as an electron blocking layer to reduce the dark-current of the detector, just as the C-TPD layer did.

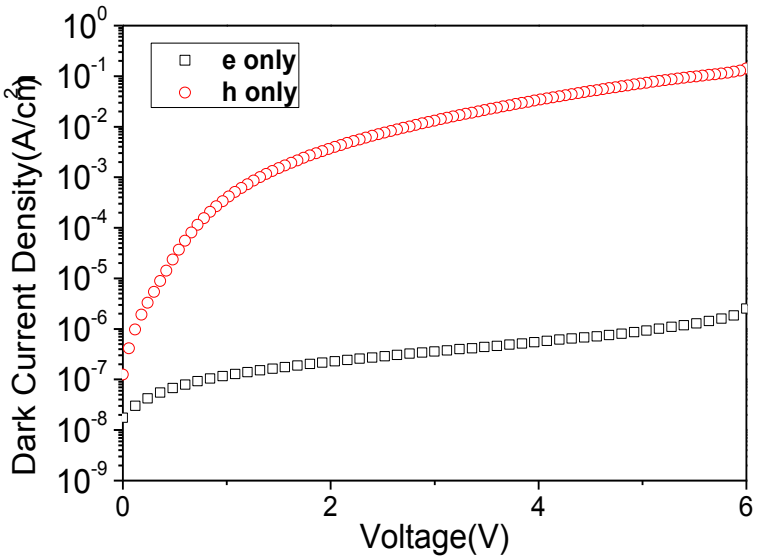

Figure 5. 6 The J-V curves of the electron-only (e-only) and hole-only (h-only) C-TPD:ZnO devices in the dark.

To further confirm the electron conductivity of the device under illumination, electron-only device was fabricated by replacing the PEDOT:PSS with Cs_2CO_3 in the original photodetector device. It is found that under the light illumination, the current density under reverse bias increases by three orders of magnitude, which demonstrates that the device changes to electron conductor under illumination, as shown in Fig.5.7.

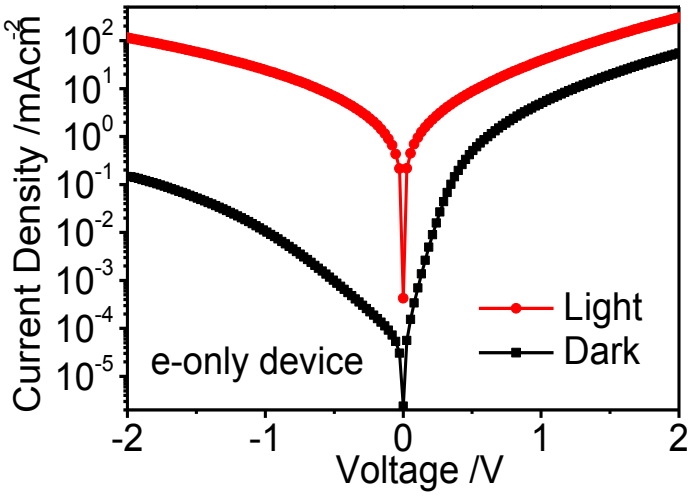

Figure 5. 7 The J-V curves of the electron-only C-TPD:ZnO/C60 device in the dark and under illumination with light intensity of 0.1 Wcm^{-2}.

In order to identify the origin of the traps in the devices, the capacitance versus frequency measurement of the UV photodetector was performed in the dark as well as under the illumination of UV or green light. During the sweeping of the frequency from high to low values, the demarcation energy is changed from below the Fermi-level, where no states can respond, to above the trap levels, where all states respond [12]. By this way, we can obtain the trap distribution in the active layers. It is shown in Fig.5.8 that under the illumination of green light, as the frequency is swept from high to low values, there is an evident inflection point at approximately 10^2 Hz; when the device is illuminated under UV light, besides the inflection point at low frequency, there is an additional one at approximately 10^4 Hz. Since ZnO only has UV response while C_{60} can respond to both UV and green light based on the absorption spectrum, we can speculate that the inflection point at high frequency corresponds to

the trap band from the ZnO layer, while the one at low frequency is related to the trap band in C_{60} layer.

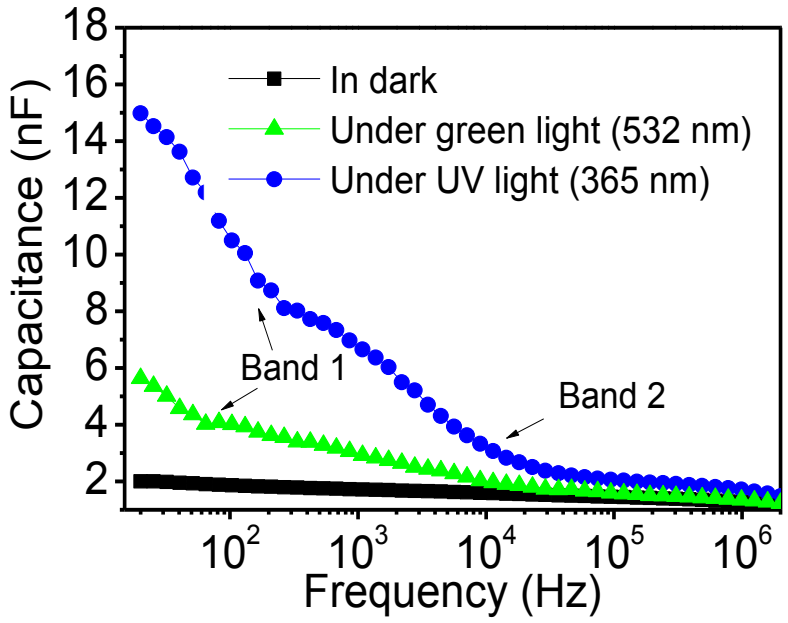

Figure 5. 8 The capacitance versus frequency curves of the device measured in the dark and under the illumination of UV or green light with light intensity of 30 $mWcm^{-2}$.

The distribution of the trap bands can be more straightforwardly presented by the calculated trap density of states verses demarcation energy curves of the device following the route proposed by Carr *et al.* [12] (Fig.5.9).

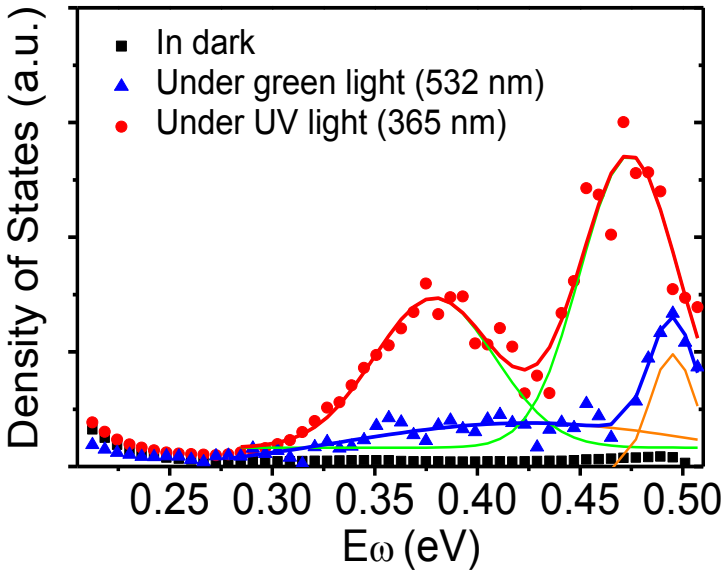

Figure 5. 9 The calculated trap density of states versus demarcation energy curves of the device fitted by the Gaussian distribution.

The demarcation energy correlates with the applied frequency by the following expression:

$$E_{\omega} = k_B T Ln \frac{\omega_0}{\omega} \tag{5.1}$$

Where ω_0 is the attempt-to-escape frequency, ω is the applied angular frequency, k_B is the Boltzmann constant, and T is the absolute temperature. For reference, an attempt-to-escape frequency of 5×10^{10} s^{-1} was used here. And the distribution of trap density of states N_T can be calculated by:

$$N_T(E_{\omega}) = -\frac{V_{bi}}{Wq}\frac{dC}{d\omega}\frac{\omega}{k_B T} \tag{5.2}$$

where V_{bi} is the build-in potential, W is the width of the depletion region, and q is the elementary charge. After fitting the curves with the Gaussian distribution, it is seen that there are two kinds of trap bands existing in the device. For the same reason

mentioned above, the deeper trap band can be attributed to the traps in the C_{60} layer, while the shallower trap band comes from the ZnO nanoparticles. The result further proves that ZnO nanoparticles bring in additional traps in the device, which can behave as the photo-switchable valve to control the electron injection.

Since the device possesses high gain and low dark-current simultaneously, it is expected to have high detectivity and should be very potential in weak light UV detection. In order to obtain the NEP value of these photodetectors, the noise current was measured by using a Stanford Research SR830 Lock-In amplifier following the route reported previously [13]. During the measurement, the lock-in frequency of the noise current was set to be 35 Hz, so that it was consistent with the frequency used in EQE measurement. The measured noise current is shown in Fig.5.10. The thermal noise limit is also shown in the figure for comparison, which is calculated by $i_{n,th} = \sqrt{4k_B TB / R}$, where B is the bandwidth, and R is the resistance of the detector. It can be seen that the noise current is extremely small and even close to the thermal noise limit under low reverse bias.

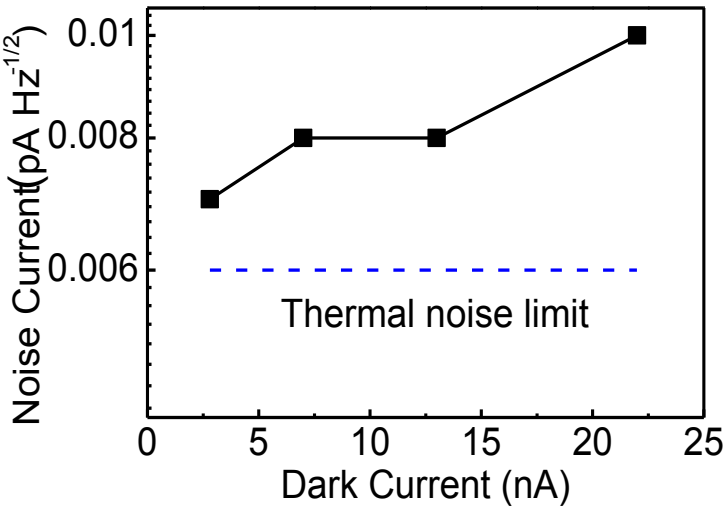

Figure 5. 10 The measured noise current under different dark-currents.

The noise current at -6 V is only 0.01 $pAHz^{-1/2}$, which is more than one order of magnitude lower than our previous device with C-TPD as the buffer layer in chapter 4. It is not clear yet why the introduction of ZnO into the buffer layer can significantly reduce the noise. Konstantatos *et al.*[13] have performed the noise current study of PbS quantum dot photodetectors with different surface oxidation degree and thus different kinds of trap states, and found that the neck-then-oxidize nanoparticle devices exhibited nearly five times lower noise current than that of the oxidize-then-neck devices. Hence, we infer that the reduced noise current in our case might also be related to the different carrier trap states in ZnO nanoparticles and in the C-TPD layer that result in different noise current levels during the carrier transportation. However, detailed noise power density spectrum study is needed in the future to explore the origin behind it. Due to the high responsivity and low noise

current, the calculated NEP of the device is only about 34 $fWHz^{-1/2}$, which shows its bright prospect in weak UV light detection.

Due to the high gain and low noise current, the peak specific detectivity of the device reaches 6.5×10^{12} Jones at 390 nm under the reverse bias of -6 V as shown in Fig.5.11, which is more than one order of magnitude larger than the device without the addition of ZnO nanoparticles in the C-TPD buffer layer. This value also approaches that of the commercial GaN UV detector, which is about 2×10^{13} Jones.

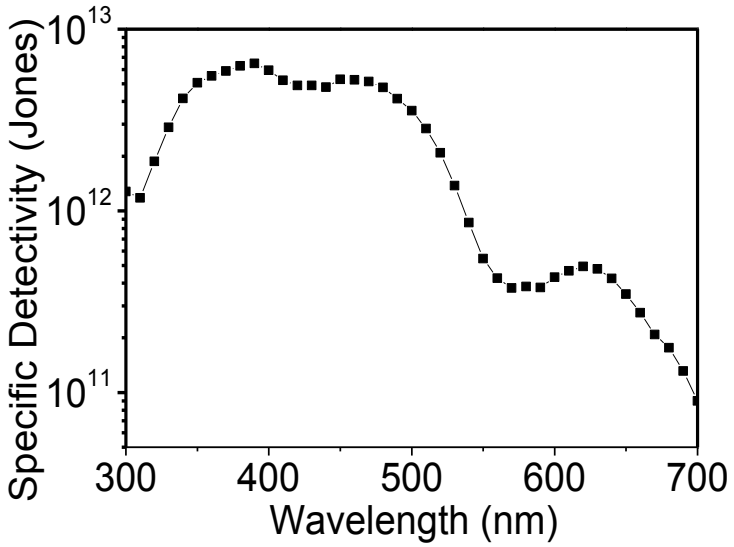

Figure 5. 11 The calculated specific detectivity of the fullerene photodetector with ZnO:C-TPD buffer layer at –6 V.

In the above calculation, the responsivity is obtained based on the EQE value measured at relatively high light intensity of 1 μWcm^{-2}. However, the responsivity may decrease with the decrease of the light intensity due to the light influence on the traps. So the low NEP calculated on the basis of the responsivity measured at high light intensity does not necessarily mean its high detectivity under very weak light illumination. One typical example is the nanocomposite photodetector lost its linearity

at weak light intensity, as shown in Chapter 3. One of the possible reasons is that ZnO nanoparticles far away from the interface do not cause useful band bending for secondary charge injection. Pushing ZnO toward the interface valve in this work should allow the very weak light to turn on the interfacial valve, and thus allow a more sensitive detection under weak light. Therefore, the linear dynamic range (LDR) of the device, which characterizes the light intensity range where the responsivity of the device keeps constant, needs to be measured to identify if the responsivity is independent of the incident light power density. The LDR was measured by recording the photocurrent at -8 V, with varied light intensities from 0.1 Wcm^{-2} all the way down to approximately 10^{-13} Wcm^{-2}, and the corresponding result is shown in Fig.5.12. It is seen that the device exhibits a linear photoresponse within the whole light intensity range used here, thus yielding a linear dynamic range of 120 dB. This value is 30 dB larger than the previous C_{60} detector with C-TPD as the buffer layer in chapter 4. This is because the device possesses much lower NEP, and at the same time does not show photocurrent saturation under illumination of high light intensity. The 120 dB LDR is significantly larger than those of the InGaAs detector [14] (66 dB) and GaN detector [15] (50 dB), better than that of the polymer photodetector (100 dB), and even comparable with that of the Si photodetector [14](120 dB). In fact, the 120 dB LDR is among the highest up-to-date LDR values for both inorganic and organic photodetectors [16]. Such good linear response of the device over a wide light intensity range is believed to be contributed by the excellent free electron generation, transportation capabilities and low electron traps of fullerene

that decrease the charge recombination probability, as well as the high light absorbance and low noise current of ZnO nanoparticles that extends the upper and lower limits of the light response range.

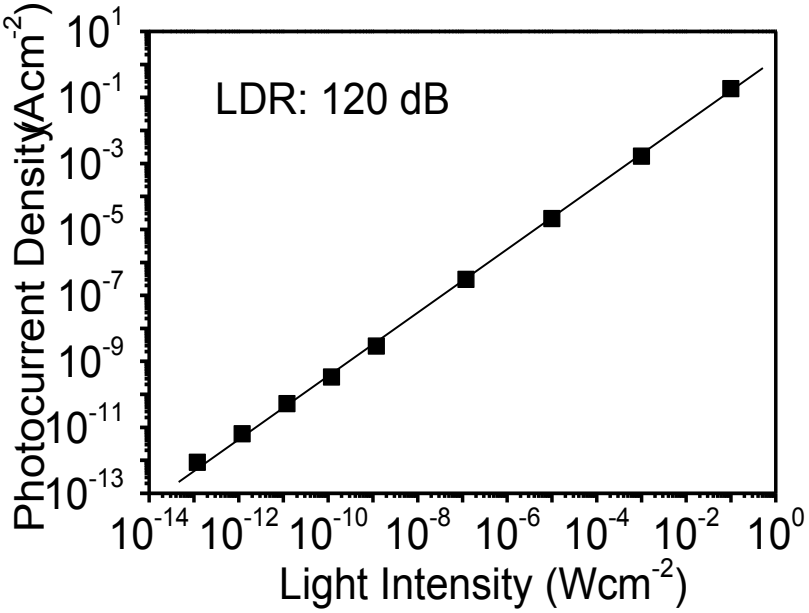

Figure 5. 12 The dynamic response of the fullerene photodetector with ZnO:C-TPD buffer layer measured with bias of –8 V.

5.4 Conclusions

In summary, the ZnO nanoparticles have been introduced into the C-TPD buffer layer of the fullerene-based UV photodetector to successfully increase the photoconductive gain and reduce the noise current. The peak EQE value of approximately 400% and the peak specific detectivity of 6.5×10^{12} Jones at the wavelength of 390 nm, along with the record high LDR of 120 dB, enable the photodetector to be used in wide range of applications such as imaging,

communication, and defense. The extremely high sensitivity of the photodetector also makes it particularly attractive for detection of weak or low light intensities.

5.5 References

[1] Guo, F., Xiao, Z. & Huang, J. Fullerene Photodetectors with a Linear Dynamic Range of 90 dB Enabled by a Cross‐Linkable Buffer Layer. *Advanced Optical Materials* **1**, 289-294 (2013).

[2] Huang, J. & Yang, Y. Origin of photomultiplication in C 60 based devices. *Applied Physics Letters* **91**, 203505-203505-203503 (2007).

[3] Reynaert, J., Arkhipov, V. I., Heremans, P. & Poortmans, J. Photomultiplication in disordered unipolar organic materials. *Advanced Functional Materials* **16**, 784-790 (2006).

[4] Fang, Y., Guo, F., Xiao, Z. & Huang, J. Large Gain, Low Noise Nanocomposite Ultraviolet Photodetectors with a Linear Dynamic Range of 120 dB. *Advanced Optical Materials* (2014).

[5] Huang, Q., Li, J., Marks, T. J., Evmenenko, G. A. & Dutta, P. Triarylamine siloxane anode functionalization/hole injection layers in high efficiency/high luminance small-molecule green-and blue-emitting organic light-emitting diodes. *Journal of applied physics* **101**, 093101 (2007).

[6] Huang, Q., Evmenenko, G. A., Dutta, P., Lee, P., Armstrong, N. R. & Marks, T. J. Covalently bound hole-injecting nanostructures. Systematics of molecular architecture, thickness, saturation, and electron-blocking characteristics on organic light-emitting diode luminance, turn-on voltage, and quantum

efficiency. *Journal of the American Chemical Society* **127**, 10227-10242 (2005).

[7] Liu, J., Qu, S., Zeng, X., Xu, Y., Gou, X., Wang, Z., Zhou, H. & Wang, Z. Fabrication of ZnO and its enhancement of charge injection and transport in hybrid organic/inorganic light emitting devices. *Applied Surface Science* **253**, 7506-7509 (2007).

[8] Pacholski, C., Kornowski, A. & Weller, H. Self‐Assembly of ZnO: From Nanodots to Nanorods. *Angewandte Chemie International Edition* **41**, 1188-1191 (2002).

[9] Jin, Y., Wang, J., Sun, B., Blakesley, J. C. & Greenham, N. C. Solution-processed ultraviolet photodetectors based on colloidal ZnO nanoparticles. *Nano letters* **8**, 1649-1653 (2008).

[10] Soci, C., Zhang, A., Xiang, B., Dayeh, S. A., Aplin, D., Park, J., Bao, X., Lo, Y.-H. & Wang, D. ZnO nanowire UV photodetectors with high internal gain. *Nano letters* **7**, 1003-1009 (2007).

[11] Guo, F., Yang, B., Yuan, Y., Xiao, Z., Dong, Q., Bi, Y. & Huang, J. A nanocomposite ultraviolet photodetector based on interfacial trap-controlled charge injection. *Nature Nanotechnology* **7**, 798-802 (2012).

[12] Carr, J. A. & Chaudhary, S. The identification, characterization and mitigation of defect states in organic photovoltaic devices: a review and outlook. *Energy & Environmental Science* **6**, 3414-3438 (2013).

[13] Konstantatos, G., Howard, I., Fischer, A., Hoogland, S., Clifford, J., Klem, E., Levina, L. & Sargent, E. H. Ultrasensitive solution-cast quantum dot photodetectors. *Nature* **442**, 180-183 (2006).

[14] Gong, X., Tong, M., Xia, Y., Cai, W., Moon, J. S. *et al.* High-detectivity polymer photodetectors with spectral response from 300 nm to 1450 nm. *Science* **325**, 1665-1667 (2009).

[15] Khan, M. A., Kuznia, J., Olson, D., Van Hove, J., Blasingame, M. & Reitz, L. High‐responsivity photoconductive ultraviolet sensors based on insulating single‐crystal GaN epilayers. *Applied Physics Letters* **60**, 2917-2919 (1992).

[16] Konstantatos, G., Clifford, J., Levina, L. & Sargent, E. H. Sensitive solution-processed visible-wavelength photodetectors. *Nature Photonics* **1**, 531-534 (2007).

CHAPTER 6 SUMMARY AND FUTURE WORK

6.1 Summary

1. We reported a new type of hybrid photodetector based on ZnO nanoparticles/polymer nanocomposite materials. The device structure is ITO/PEDOT:PSS/TPD:PVK/ZnO:Polymer/BCP/Al. It is a diode in the dark and a photoconductor under ultraviolet illumination. Through the interfacial-trap controlled charge injection, the device has shown tens to hundreds of times better detectivity than inorganic semiconductor photodetectors. The peak external quantum efficiency is 245,300% and 340,600% under bias of -9 v at 360 nm for the PVK:ZnO and P3HT:ZnO devices, respectively; The peak responsivities, at illumination light intensity of 1.25 $\mu W/cm^2$, are 721 A/W for the PVK:ZnO device and 1001 A/W for the P3HT:ZnO device at 360 nm, which are more than three orders of magnitude larger than that of commercial GaN or SiC detectors; At illumination light intensity of 1.25 $\mu W/cm^2$, the specific detectivities at 360 nm are 3.4×10^{15} Jones for PVK:ZnO devices and 2.5×10^{14} Jones for P3HT:ZnO devices. The specific detectivities in the UV range are 2-3 orders of magnitude larger than silicon and GaN UV detectors. The specific detectivity of a P3HT:ZnO device within the visible light range is also more than ten times better than that of silicon detectors; The 3-dB bandwidth is 9.4 kHz. The devices provide over

10^5 fold improvement in gain-bandwidth product in solution-processed ZnO UV photodetection relative to previous reports. These thin-film photodetectors have great potential for the existing applications in very weak UV and visible light detection and can potentially open new application opportunities because of their flexibility, light weight and low cost, compared to the traditional inorganic semiconductor devices.

2. We designed a high sensitivity ultraviolet photodetector based on fullerene materials. The dark-current of the photodetector has been successfully reduced by 3-4 orders of magnitude with a C-TPD buffer layer. The device structure is ITO/PEDOT:PSS/C-TPD/C60/BCP/Al. The high detectivity of 3.6×10^{11} Jones at 370 nm and the wide LDR of 90 dB, along with a response speed faster than 20 kHz, suggests that the fullerene-based organic photodetectors reported here can open the way for many potential applications, such as replacing the CCD array in a digital camera. The high sensitivity of this type of photodetector, particularly in the UV range, makes it potentially useful in monitoring the weak UV emission from scintillators which generally give UV emission.
3. The ZnO nanoparticles have been introduced into the C-TPD buffer layer of the fullerene-based photodetector to successfully increase the photoconductive gain and reduce the noise current. The device has a structure of ITO/PEDOT:PSS/C-TPD:ZnO/C60/BCP/Al. The peak EQE value of approximately 400% and the peak specific detectivity of 6.5 ×1012 Jones at the

wavelength of 390 nm, along with the record high LDR of 120 dB, enable the photodetector to be used in wide range of applications such as imaging, communication, and defense. The extremely high sensitivity of the photodetector also makes it particularly attractive for very weak light detection.

6.2 Future Works

1. The synthesis of ZnO nanostructures is still challenging. Since ZnO nanoparticles play critical roles in the photodeector, the parameters of the ZnO nanoparticles, including diameter, shape, orientation, density, and crystallization, will affect the performances of the photodetector. Additional works are needed to confirm the relationship between ZnO nanoparticle parameters and device performances.
2. For the ZnO/Polymer nanocomosite photodetector, the photoconductive gain decreases at ultralow light intensity, this is a disadvantage in the application of weak light detection. It was possibly caused by the non-ideal distribution of ZnO nanoparticles. Those ZnO nanoparticles that located far away from the cathode won’t induce as much Schottky junction-narrowing effect as those close to the cathode side. It might be beneficial if more ZnO nanoparticles can be pushed to the cathode side. Deposit a pure ZnO nanoparticle layer on top of the active layer at the cathode side is a possible solution.

3. For the fullerene photodetector with ZnO:C-TPD buffer layer, the noise current was found sometimes below the shot noise limit. This phenomenon cannot be explained at current stage. Further works are needed to explore it.
4. The device degradation mechanism has not been studied yet and need further study in the future.

LIST OF PUBLICATIONS

[1] Guo, F., Yang, B., Yuan, Y., Xiao, Z., Dong, Q., Bi, Y. & Huang, J. A nanocomposite ultraviolet photodetector based on interfacial trap-controlled charge injection. *Nature Nanotechnology* **7**, 798-802 (2012).

[2] Guo, F., Xiao, Z. & Huang, J. Fullerene Photodetectors with a Linear Dynamic Range of 90 dB Enabled by a Cross-Linkable Buffer Layer. *Advanced Optical Materials* **1**, 289-294 (2013).

[3] Guo, F., Fink, T., Han, M., Koester, L., Turner, J. & Huang, J. High-sensitivity, high-frequency extrinsic Fabry–Perot interferometric fiber-tip sensor based on a thin silver diaphragm. *Optics Letters* **37**, 1505-1507 (2012).

[4] Fang, Y., Guo, F., Xiao, Z. & Huang, J. Large Gain, Low Noise Nanocomposite Ultraviolet Photodetectors with a Linear Dynamic Range of 120 dB. *Advanced Optical Materials* (2014).

[5] Yang, B., Guo, F., Yuan, Y., Xiao, Z., Lu, Y., Dong, Q. & Huang, J. Solution-Processed Fullerene-Based Organic Schottky Junction Devices for Large-Open-Circuit-Voltage Organic Solar Cells. *Advanced Materials* **25**, 572-577 (2013).

[6] Yuan, Y., Dong, Q., Yang, B., Guo, F., Zhang, Q., Han, M. & Huang, J. Solution-processed nanoparticle super-float-gated organic field-effect transistor as un-cooled ultraviolet and infrared photon counter. *Scientific reports* **3** (2013).

[7] Yang, B., Cox, J., Yuan, Y., Guo, F. & Huang, J. Increased efficiency of low band gap polymer solar cells at elevated temperature and its origins. *Applied Physics Letters* **99**, 133302 (2011).

[8] Han, M., Guo, F. & Lu, Y. Optical fiber refractometer based on cladding-mode Bragg grating. *Optics Letters* **35**, 399-401 (2010).

[9] Guo, F. & Huang, J. in *SPIE Defense, Security, and Sensing.* 83732K-83732K-83712 (International Society for Optics and Photonics).

[10] Rui Dong, C. B., Qingfeng Dong, Fawen Guo, Yongbo Yuan, Yanjun Fang, Zhengguo Xiao,Jinsong Huang. An Ultraviolet-to-NIR Broad Spectral Nanocomposite Photodetector with Gain. *Advanced Optical Materials* (2014).